

Multiple mechanisms for licensing human replication origins

<https://doi.org/10.1038/s41586-024-08237-8>

Ran Yang^{1,2}, Olivia Hunker^{1,2}, Marleigh Wise¹ & Franziska Bleichert^{1,2}✉

Received: 15 February 2024

Accepted: 16 October 2024

Published online: 27 November 2024

 Check for updates

Loading of replicative helicases is obligatory for the assembly of DNA replication machineries. The eukaryotic MCM2–7 replicative helicase motor is deposited onto DNA by the origin recognition complex (ORC) and co-loader proteins as a head-to-head double hexamer to license replication origins. Although extensively studied in budding yeast^{1–4}, the mechanisms of origin licensing in multicellular eukaryotes remain poorly defined. Here we use biochemical reconstitution and electron microscopy to reconstruct the human MCM loading pathway. We find that unlike in yeast, the ORC6 subunit of the ORC is not essential for—but enhances—human MCM loading. Electron microscopy analyses identify several intermediates en route to MCM double hexamer formation in the presence and absence of ORC6, including a DNA-loaded, closed-ring MCM single hexamer intermediate that can mature into a head-to-head double hexamer through multiple mechanisms. ORC6 and ORC3 facilitate the recruitment of the ORC to the dimerization interface of the first hexamer into MCM–ORC (MO) complexes that are distinct from the yeast MO complex^{5,6} and may orient the ORC for second MCM hexamer loading. Additionally, MCM double hexamer formation can proceed through dimerization of independently loaded MCM single hexamers, promoted by a propensity of human MCM2–7 hexamers to self-dimerize. This flexibility in human MCM loading may provide resilience against cellular replication stress, and the reconstitution system will enable studies addressing outstanding questions regarding DNA replication initiation and replication-coupled events in the future.

Accurate and timely bidirectional replication of genomic DNA is essential for the coordination of genome and cell duplication and the flow of genetic information to progeny. To ensure once-per-cell-cycle genome replication, eukaryotic cells have evolved a cell cycle-regulated, two-step replication initiation process^{4,7}. First, origins are licensed by loading two copies of the hexameric minichromosome maintenance 2–7 (MCM2–7) replicative helicase motor onto replication origin DNA, which results in the formation of head-to-head MCM double hexamers^{8–10}. In the second initiation step—origin firing—MCM double hexamers mature into active, bidirectional replication forks.

Bidirectionality of eukaryotic DNA replication is established during MCM double hexamer formation and relies on the loading of two MCM2–7 hexamers in opposing orientations. Biochemical reconstitution of origin licensing with purified *Saccharomyces cerevisiae* proteins have illuminated the mechanisms of budding yeast MCM double hexamer assembly^{1–3}. In this model (Fig. 3a), the heterohexameric ORC binds to specific origin DNA sequences in an ATP-dependent manner^{11,12} and enables association of the co-loader Cdc6¹³. The ORC–Cdc6–DNA complex recruits the first MCM hexamer, along with Cdt1, leading to the formation of an OCCM (ORC–Cdc6–Cdt1–MCM) intermediate, in which the first MCM hexamer topologically encircles DNA^{14,15}. Following the release of Cdc6 and Cdt1—the latter event being coupled to ATP hydrolysis by MCM^{16–18}—the MO intermediate is formed⁵; either

the same ORC flips to an inverted secondary DNA binding site at the opposite face of the first loaded Mcm2–7 hexamer⁶, or a second ORC diffuses in to bind at this site⁵. Orc6 has a critical role in establishing the *S. cerevisiae* MO by stabilizing the first loaded MCM hexamer on DNA and bridging the interface between MCM and ORC^{5,6,19}. Further, in the ORC flip model, a long flexible linker in Orc6 is likely to tether the ORC to MCM during repositioning⁶. The MO complex then recruits and loads the second MCM hexamer through the OCCM mechanism^{5,6}.

Considerably less is known about how origin licensing occurs in other eukaryotes. Several key differences between yeast and human ORCs suggest that human MCM loading may diverge from that of budding yeast: (1) the ORC in most eukaryotes does not bind to a defined origin sequence as in budding yeast^{20,21}; (2) unlike yeast Orc6, metazoan ORC6 proteins (*Drosophila* being an exception) do not stably associate with the core ORC1–5 subunits^{22–25}; and (3) they lack the very long flexible linker that is probably utilized by yeast Orc6 for ORC flipping and MO formation²⁴. Moreover, MCM double hexamers purified from human cells encircle partially melted rather than fully base-paired DNA as the budding yeast counterpart^{26–28}, suggesting the possibility of distinct mechanisms for double hexamer formation. The lack of full biochemical reconstitution of human replication initiation has hampered progress towards understanding human origin licensing and firing mechanisms.

¹Department of Molecular Biophysics and Biochemistry, Yale University, New Haven, CT, USA. ²These authors contributed equally: Ran Yang, Olivia Hunker. [✉]e-mail: franziska.bleichert@yale.edu

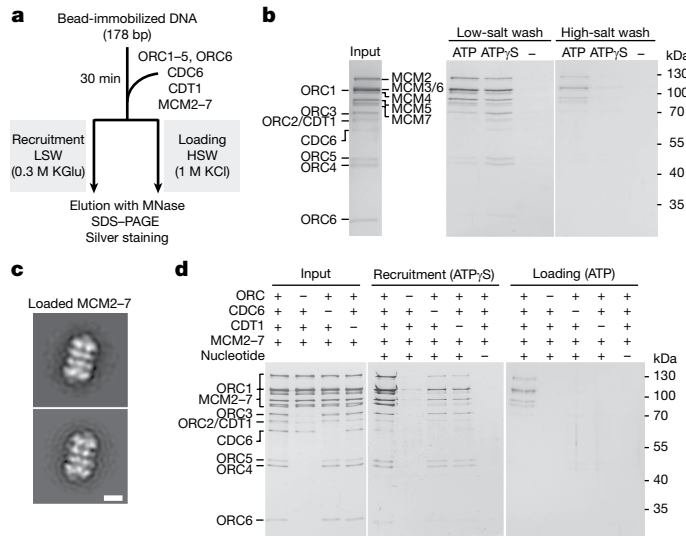


Fig. 1 | In vitro reconstitution of human MCM loading. **a**, Schematic outline of bead-based human MCM recruitment and loading assays. KGl, potassium glutamate. HSW, high-salt wash; LSW, low-salt wash. Elution with MNase, elution by micrococcal nuclease (MNase) digestion. **b**, Nucleotide-dependent recruitment and loading of human MCM2–7. SDS-PAGE with silver staining. **c**, Loaded MCM2–7 complexes are double hexamers. Two-dimensional EM class averages of negatively stained particles eluted from beads after high-salt wash. Scale bar, 10 nm. **d**, MCM loading requires the ORC, CDC6 and CDT1. SDS-PAGE with silver staining of inputs and eluates after low- (recruitment) and high-salt wash (loading). Full-length loading factors were used in these experiments. In **b,d**, solidus indicates that proteins migrate at the same position. For gel source data, see Supplementary Information.

Reconstitution of human origin licensing

To examine how human MCM double hexamers are loaded onto DNA, we developed an in vitro reconstitution strategy similar to the one established for budding yeast and *Drosophila* models^{8,9,29}. Unlike MCM loading intermediates, MCM double hexamers are salt-stable; thus, MCM loading can be distinguished from MCM recruitment to DNA by differential salt washes (Fig. 1a). We combined purified human ORC1–5, ORC6, CDC6, CDT1 and MCM2–7 with bead-immobilized DNA in the absence or presence of nucleotide and assessed MCM recruitment and loading after low-salt and high-salt washes, respectively (Fig. 1a). As in budding yeast initiation^{8,9}, recruitment of human MCM2–7 and other loading factors was observed with both ATP and the slowly hydrolysable nucleotide analogue ATP γ S, whereas substantial MCM loading was seen only in reactions with ATP, indicating a requirement of ATP hydrolysis for efficient MCM loading (Fig. 1b; hereafter, we use only ATP γ S for recruitment reactions). MCM2–7 that eluted from beads in ATP reactions resembled double hexamers in electron microscopy (EM) images, confirming successful MCM loading (Fig. 1c and Extended Data Fig. 1a).

Omission of the initiator ORC or the co-loaders CDC6 or CDT1 prevented salt-stable retention of MCM2–7 on DNA; however, a small amount of MCM2–7 could be recruited without CDC6 or CDT1, but not without the ORC (Fig. 1d). Whereas these licensing factors were required for human MCM loading, the intrinsically disordered regions (IDRs) in ORC1, CDC6 and CDT1 that promote liquid–liquid phase separation and localization to chromatin^{30,31} were not, as previously seen with the fly proteins²⁹ (Extended Data Fig. 1b). Notably, addition of human geminin, a metazoan-specific origin licensing inhibitor that sequesters CDT1^{32,33}, impedes both MCM recruitment and loading (Extended Data Fig. 1c,d). Thus, we conclude that our biochemical in vitro reconstitution reflects bona fide origin licensing.

To improve the versatility of our reconstituted system, we used truncated ORC1 and CDT1 constructs in subsequent experiments, as removal of their IDRs substantially improved the purification yield of these proteins. Moreover, we developed a fluorescence-based bead assay that leverages GFP-tagged MCM to enable more precise quantification of MCM recruitment and loading (Extended Data Fig. 1e–h). With these tools, we set out to explore how MCM is loaded onto DNA during human origin licensing.

ORC6 is dispensable for MCM loading

Next, we assessed the contributions of individual ORC subunits to human MCM loading. Although the ORC is needed for MCM loading in yeast, the strict requirement of some ORC subunits for human origin licensing has been debated^{34–37}. We found that an ORC that lacks ORC1 (ORC2–5) could not recruit or load MCM; these defects were not rescued by excess CDC6, an ORC1 parologue that has been suggested to partially compensate for the lack of ORC1 (refs. 34,37) (Extended Data Fig. 2a). By contrast, ORC6 was not essential for the deposition of human MCM2–7 onto DNA, although this subunit considerably stimulated MCM loading but not recruitment (Fig. 2a and Extended Data Fig. 2b). Of note, MCM double hexamers loaded in the absence of ORC6 appeared structurally similar in 2D class averages to those loaded with ORC6 (Fig. 2b). Quantification of the number of salt-stable double hexamers in negative-stain EM images of loading reaction eluates revealed an increase of around tenfold when ORC6 was included (Fig. 2c). The ORC6-mediated enhancement of MCM loading required all ORC6 protein domains in *cis* on the same polypeptide (Extended Data Fig. 2c–g). However, the need for ORC6 for efficient MCM double hexamer formation could be overcome by increasing concentrations of the ORC and CDC6 (Fig. 2d–f). Collectively, these results define the minimal components of our in vitro origin licensing system and establish that ORC1, but not ORC6, is essential for human MCM loading. Although ORC6 stimulates this event (especially at low ORC and CDC6 concentrations), its dispensability was unexpected because *S. cerevisiae* Orc6 is essential for origin licensing^{38–40}, raising fundamental questions regarding the loading mechanism of human MCM both in the presence and absence of ORC6.

EM of the human MCM loading pathway

Several intermediates en route towards MCM double hexamer formation have been identified and structurally characterized in the budding yeast system, including the OCCM^{14,15} and MO^{5,6} complexes (Fig. 3a). To define whether the same intermediates are formed during human MCM loading, we analysed our MCM loading reactions with ORC6 (as it stimulates MCM loading) by negative-stain EM (Fig. 3b). ORC and CDC6 concentrations (120 nM) were chosen so that they align with nuclear ORC concentrations (around 15–200 nM) estimated by mass spectrometry⁴¹ and so that loading reactions could be imaged without diluting samples.

Two-dimensional classification revealed that almost 50% of MCM hexamers had been incorporated into double hexamer particles (MCM-DH) in the presence of ATP (Fig. 3c,d). In addition to the free ORC, free (non-loaded) MCM2–7 and MCM-DH particles, we also identified a small number of OCCM intermediates (which were enriched in the presence of ATP γ S), as well as around 10% of MCM as single hexamer particles (MCM-SH) that closely resembled the hexamers in MCM-DH (Fig. 3c,d). MCM-SH class averages were not observed with MCM2–7 alone or at the beginning of the loading reaction, indicating these particles corresponded to loaded MCM single hexamers (Extended Data Fig. 3a). Notably, a subset of class averages was composed of the ORC attached to the N-terminal face of an MCM2–7 hexamer, and these classes were dependent on the presence of DNA in the reaction (Fig. 3c,d and Extended Data Fig. 3b). Although this organization is

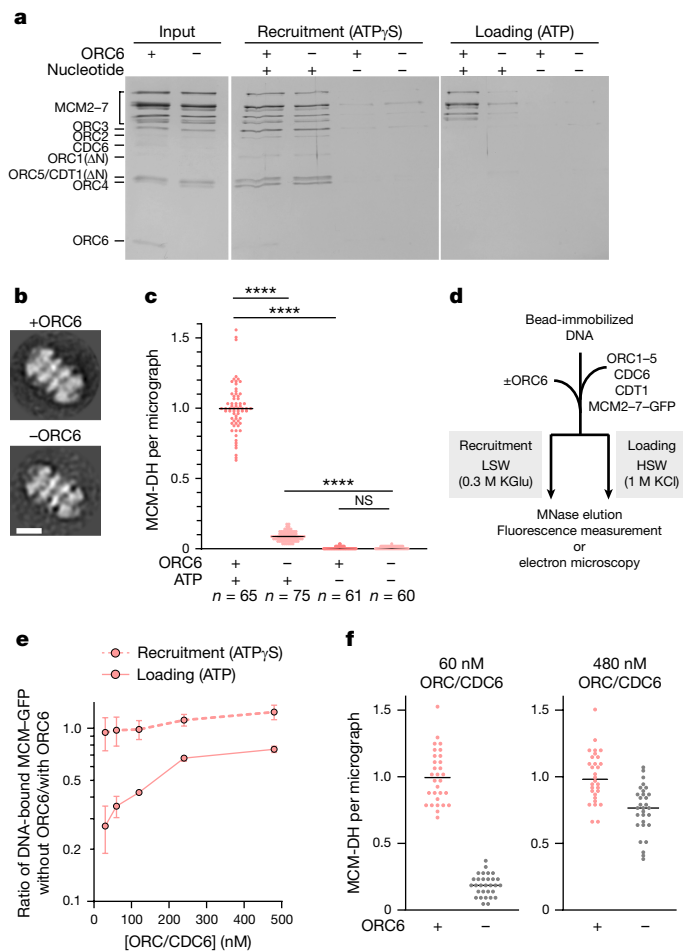


Fig. 2 | ORC6 is dispensable for human MCM loading in vitro but increases loading efficiency. **a**, SDS-PAGE with silver staining of elutions from bead-based MCM recruitment and loading assays with and without ORC6. Solidus indicates that proteins migrate at the same position. **b**, Two-dimensional EM class averages of negatively stained particles from elutions of loading reactions show that MCM2-7 complexes loaded onto DNA without ORC6 are double hexamers. Scale bar, 10 nm. **c**, Quantification of MCM double hexamers (MCM-DH) observed per micrograph from loading reactions with and without ORC6. MCM-DH counts per micrograph were normalized to the average seen with ATP and ORC6. The total number of micrographs (*n*) analysed from three independent experiments is listed. Two-way ANOVA with Tukey's multiple comparisons test. **d–f**, Increasing ORC and CDC6 (ORC/CDC6) concentration overcomes the requirement for ORC6 in efficient MCM loading. **d**, Schematic of experimental workflow in **e,f**. **e**, Ratios of GFP fluorescence intensities in elutions of bead-based recruitment and loading reactions without and with ORC6 at a given ORC/CDC6 concentration. ORC6 was equimolar to ORC1-5 when included. Data are mean ± s.d. from three independent experiments. **f**, MCM double hexamer counts per electron micrograph in elutions from loading reactions at 60 nM and 480 nM ORC/CDC6 (with or without ORC6) normalized to the respective reaction with ORC6. Ten micrographs for each of the three independent experiments (total *n* = 30) were analysed for each condition. For gel and micrograph source data, see Supplementary Information. Horizontal lines in **c,f** represent means. *****P* < 0.0001; NS, not significant.

reminiscent of the yeast MO intermediate, comparison of these class averages with 2D projections of the yeast MO suggests that the human complex may be structurally distinct, with the ORC being oriented differently towards MCM (thus 'MO-like'; compare Fig. 3c and Extended Data Fig. 3c).

To gain higher-resolution information on structural transitions during human MCM loading, we subjected in vitro ATP-loading reactions (with ORC6) to cryo-EM analysis. Although the MO-like complexes were

of insufficient abundance for cryo-EM structure determination, our data yielded structures of loaded MCM single and double hexamers at 3.4 and 2.8 Å resolution, respectively (Fig. 3e–h, Extended Data Figs. 4 and 5 and Extended Data Table 1). Several features of these structures are noteworthy. First, the gates at the MCM2–MCM5 interface that serve as the entry site for DNA during loading⁴² are fully closed in both structures, and no additional density is seen near this gate in the MCM-SH cryo-EM map (Fig. 3e,g); in the yeast MO, Orc6 latches across the Mcm2/5 gate and stabilizes the loaded MCM single hexamer on DNA^{5,19}. Second, DNA is bound in the central pore of both single and double MCM hexamer structures (Fig. 3f,h,i and Extended Data Fig. 5f). DNA in the cryo-EM map of MCM-SH is fully base-paired, whereas one base pair is broken at the hexamer interface in MCM-DH, as in the previous structure of endogenous MCM double hexamers from human cells²⁶ (Fig. 3f,h,i). Thus, DNA underwinding and base pair melting occur during MCM double hexamer formation, and the distinct DNA conformations seen in prior human and budding yeast double hexamer structures are not caused by disparate sample preparation strategies (*S. cerevisiae*: in vitro reconstituted, no DNA melting^{27,28}; human: purified from cells, DNA melting²⁶), but represent species-specific differences. Third, the ATPase sites in our MCM-SH and MCM-DH structures have identical nucleotide occupancies with five of them having hydrolysed or released nucleotide (Fig. 3j). These post-catalytic states are consistent with ATP hydrolysis by MCM coinciding with single hexamer loading events, as established for *S. cerevisiae*^{16–18}, but differ from the ATPase configuration in the endogenously purified human MCM-DH²⁶, implying that nucleotide can exchange at some of these sites after loading (Extended Data Fig. 6a–c).

ORC6 and ORC3 promote human MO assembly

Our initial negative-stain EM analysis of human MCM loading reactions indicated the formation of an MO-like complex that appeared structurally distinct from the *S. cerevisiae* MO intermediate (Fig. 3c and Extended Data Fig. 3c). As we were unable to obtain a 3D cryo-EM reconstruction of the human MO-like complex from our ATP-loading reaction datasets, we used particles in negative-stain MO-like classes to reconstruct a low-resolution 3D map of this complex. Docking of the ORC and MCM2-7 structures into this map confirmed the different orientations of the ORC and MCM compared with the yeast MO (Extended Data Fig. 3d–f). When examining the temporal relationship of the human MO-like complex to other MCM loading assemblies by negative-stain EM, we found that MO-like particles accumulate early during the MCM loading reaction before MCM double hexamers are observed, peak 5 min after ATP addition, and then diminish (Extended Data Fig. 3g,h). The appearance of MO-like particles closely correlated with that of loaded MCM-SH, implying that MO-like complex formation is linked to the loading of single hexamers.

Next, we tested whether human MO-like complexes are involved in: (1) loading of one or both MCM hexamers onto DNA; and (2) the ORC6-mediated stimulation of MCM double hexamer formation (Fig. 2). To this end, we collected negative-stain EM datasets of MCM loading reactions (at 30 min) performed with ATP or ATP_yS, and with or without ORC6, and quantified the number of MCM hexamers in OCCM, MCM-SH, MO-like and MCM-DH 2D classes (Fig. 4a). Substituting ATP_yS for ATP did not completely block MCM loading at the OCCM stage, but instead led to accumulation of MCM-SH and MO-like particles, as well as some MCM double hexamers (Fig. 4a). Although we cannot rule out that ATP_yS is inefficiently hydrolysed at some of the MCM ATPase sites, these observations suggest that transitioning past the OCCM stage can to some extent be uncoupled from ATP hydrolysis in the human system; however, both events probably coincide in the presence of ATP, considering that our DNA-loaded, MCM-SH cryo-EM structure is in the post-catalytic state (Fig. 3j and Extended

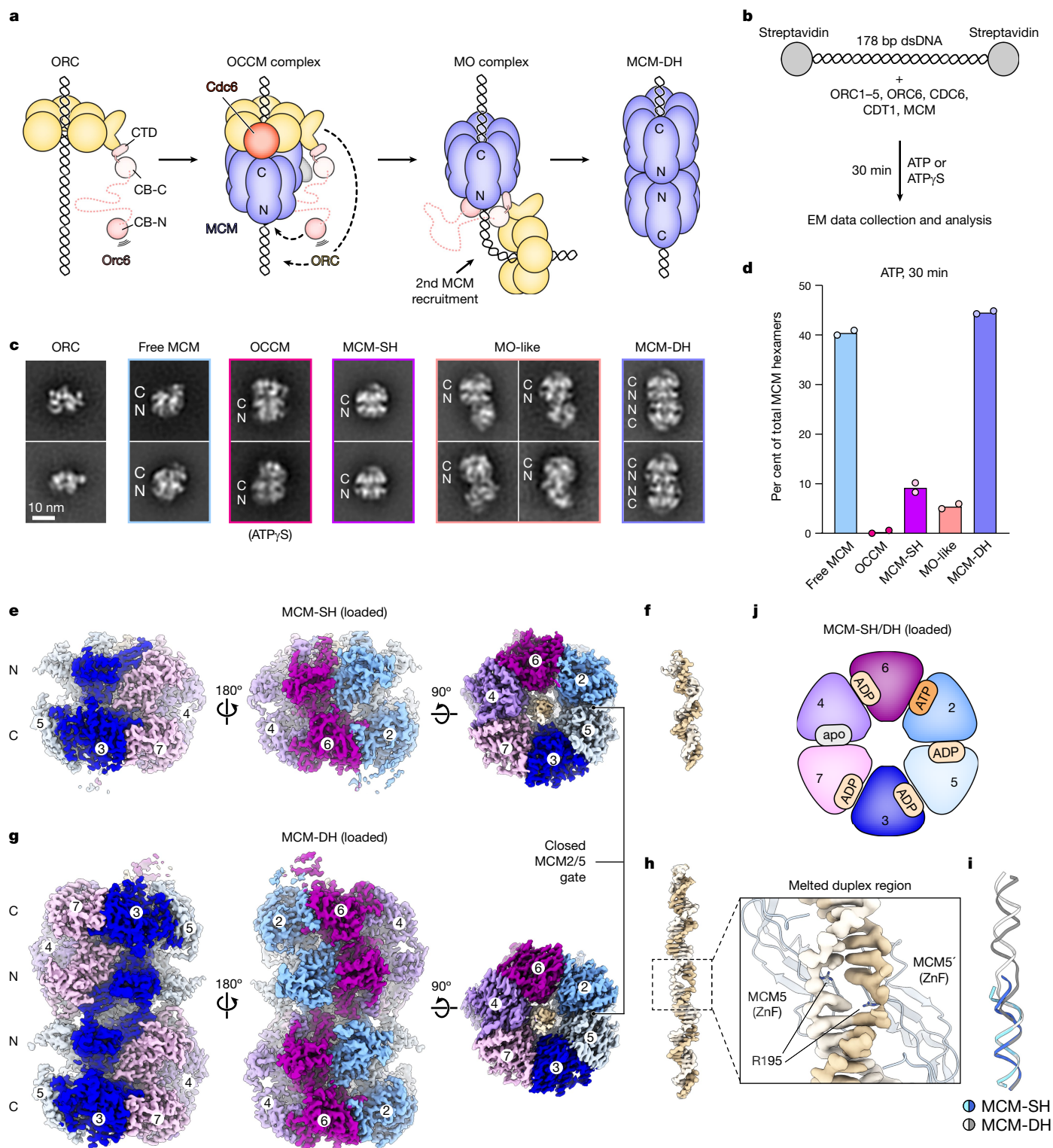
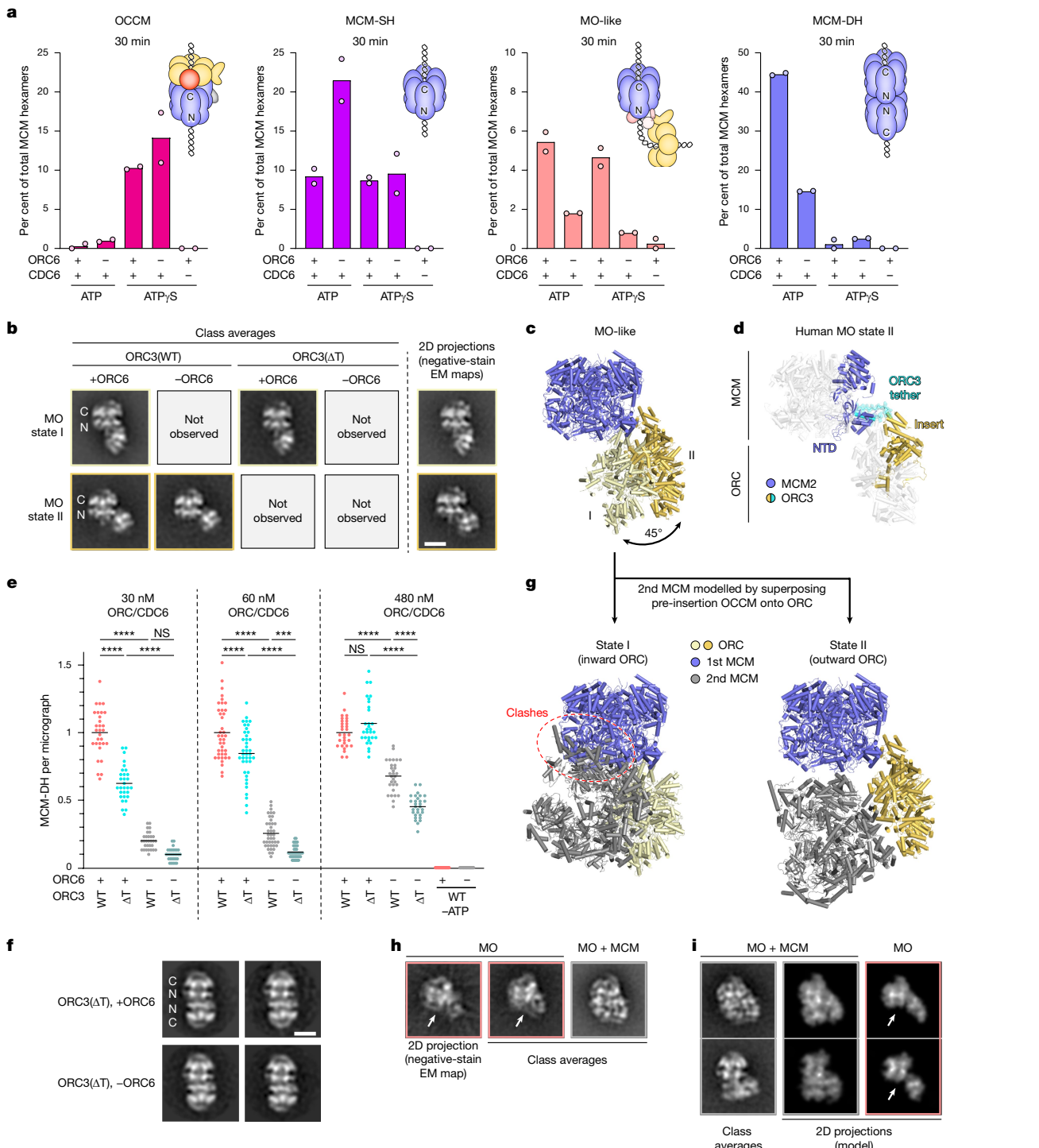


Fig. 3 | EM reveals multiple intermediates during human MCM loading.

a, A subset of MCM loading intermediates structurally characterized in *S. cerevisiae*. CB-N, N-terminal cyclin-box fold; CB-C, C-terminal cyclin-box fold; CTD, C-terminal domain. **b**, Experimental workflow for analysing human MCM loading reactions by negative-stain EM. **c**, Representative class averages of human MCM loading intermediates. The location of N- and C-terminal tiers in MCM2–7 are marked with N and C. **d**, Quantification of human MCM2–7-containing assemblies after 30 min loading with ATP from 2 independent loading reactions. Note that the percentage of MCM-SH is likely to be an underestimate, as non-side views could not be unambiguously distinguished from free MCM and were therefore counted as free MCM. **e,f**, Cryo-EM

structure of DNA-loaded human MCM single hexamers (MCM-SH): sharpened MCM-SH cryo-EM map (**e**) and cryo-EM map density for DNA in the central MCM pore (**f**). Both DNA strands are fully base-paired. **g,h**, Cryo-EM structure of DNA-loaded human MCM double hexamers (MCM-DH): sharpened MCM-DH cryo-EM map (**g**) and cryo-EM map density for DNA inside loaded double hexamers (**h**). R195 in the zinc-finger (ZnF) of MCM5 stabilizes the melting of one base pair at the dimerization interface of in vitro loaded MCM2–7. **i**, Superposition of DNA duplexes from loaded MCM single and double hexamers illustrates underwinding and melting of the DNA duplex in MCM-DH. **j**, Nucleotide states in loaded single and double hexamers (viewed from the C-terminal MCM tier).

**Fig. 4 | Human ORC6 and ORC3 stimulate assembly of an MO-like complex.**

a, Quantification of MCM-containing assemblies by negative-stain EM after 30 min loading reactions with or without ORC6 in ATP or ATP_yS (at 120 nM ORC/CDC6). Two independent experiments with 100–150 micrographs each were analysed per condition. **b**, Negative-stain EM 2D class averages of MO particles in two distinct structural states in loading reactions with and without ORC6 and an ORC3 tether deletion mutant (ORC3(ΔT)). WT, wild type. Scale bar, 10 nm. **c**, Superposition of MCM in both structural models of the human MO-like complex. **d**, AlphaFold Multimer prediction of an interaction between a tether region in the ORC3 insert and the MCM2 N-terminal domain (NTD). **e**, Quantification of MCM-DH particles in elutions of bead-based loading reactions with or without ORC6 and ORC3(WT) or ORC3(ΔT). MCM-DH numbers per micrograph were normalized to the +ORC6, ORC3(WT) reaction for each ORC/CDC6 concentration. Ten micrographs were analysed per condition and

independent experiment (total $n = 30$ for 30 nM and 480 nM ORC/CDC6; total $n = 40$ for 60 nM ORC/CDC6 reactions). Horizontal lines represent means.

Two-way ANOVA and Tukey's multiple comparison tests. *** $P < 0.0001$; ** $P = 0.0006$; NS, not significant. For recruitment, see Extended Data Fig. 3m.

f, Two-dimensional class averages of MCM-DHs loaded in reactions with ORC3(ΔT). Scale bar, 10 nm. **g**, Modelling of a second MCM by superposing the ORC from the yeast pre-insertion OCCM (Protein Data Bank (PDB) 6WGG⁴³) onto the ORC in the human MO-like complexes. **h**, Two-dimensional projection of MO state II negative-stain EM map and two classes corresponding to the same view of the MO, with extra density in the right one (MO + MCM). **i**, Comparison of class averages of a putative MO with a second MCM complex with 2D projections generated from a modelled complex and with the MO only (state II). Arrows in **h**, **i** mark the region in MO class averages or projections occupied by a second MCM hexamer in the MO + MCM images.

Data Fig. 6c). By contrast, ATP hydrolysis is required for efficient maturation of single MCM hexamers to double MCM hexamers. Reactions without ORC6 supported the assembly of double hexamers with ATP, but at reduced levels, in agreement with bead-based MCM loading assays (Fig. 4a). Accumulation of OCCM was not negatively affected in no-ORC6 reactions, indicating that ORC6 is not required for human OCCM assembly; this result is consistent with the efficient recruitment of loading factors to DNA in bead assays in the absence of this ORC subunit (Fig. 2a and Extended Data Fig. 2b,f). By contrast, ORC6 omission led to an approximately twofold increase in loaded MCM-SH particles in the ATP condition and a strong reduction in the number of MO-like complexes (Fig. 4a). Of note, the appearance of MCM-SH and MO-like classes was dependent on OCCM formation and mostly negligible in ATP γ S reactions without CDC6 (an essential component of OCCM; compare bars 3 and 5 in Fig. 4a). Collectively, these results suggest that the MO-like complex acts after the OCCM and MCM single hexamer loading but prior to double hexamer formation in the loading pathway.

Our data indicated that assembly of MO-like complexes was facilitated by ORC6; yet, in the absence of ORC6, we still observed a small number of MO-like particles in which the ORC appeared to be positioned near the edge rather than the centre of the N-terminal face of a loaded MCM single hexamer (Fig. 4b). Combining MO-like particles from multiple datasets yielded a low-resolution map of a second MO-like state, in which the ORC had rotated outwards by around 45° (Fig. 4c, state II and Extended Data Fig. 3i,j). AlphaFold modelling predicts that the interaction between MCM and ORC in this second state is stabilized by a loop–helix region in the ORC3 insert domain that binds MCM2 (Fig. 4d and Extended Data Fig. 3k,l). Deletion of this ‘tether’ in ORC3(ORC3(Δ T)) abrogated formation of the MO-like state II complex (Fig. 4b). When omitting ORC6 from loading reactions with ORC3(Δ T), we observed no MO-like particles, consistent with ORC6 and the ORC3 tether mediating the assembly of two distinct MO-like states (Fig. 4b). The ORC3 tether also contributed to MCM loading in canonical loading assays, although to a lesser extent than ORC6 (Fig. 4e,f and Extended Data Fig. 3m,n). Removing the ORC3 tether and ORC6 at the same time still supported MCM loading at higher ORC/CDC6 concentration (Fig. 4e). Thus, although both MO-like states appear to stimulate MCM loading, neither is strictly required.

We initially presumed that the human MO-like complex performed an analogous function to the yeast MO⁵, recruiting a second MCM hexamer to an already loaded first hexamer; however, this assumption is challenged by the distinct orientations of the ORC with respect to the MCM2–7 hexamer compared with the yeast MO (Extended Data Fig. 3d–f,i,j). Modelling of a second MCM hexamer by superposition of the ORC from the budding yeast pre-insertion OCCM structure⁴³ onto the docked ORC models in the human MO-like 3D reconstructions revealed major clashes between the two MCM2–7 rings in MO state I but not in MO state II, suggesting that the state II conformation might facilitate canonical MO-mediated recruitment of a second MCM hexamer as seen with the budding yeast MO (Fig. 4g). Indeed, 2D projections generated from a modelled MCM–OCCM complex using MO-like state II resembled a few very rare class averages that could not be accounted for by other loading intermediates (Fig. 4h,i). These analyses indicate that, despite their distinct architectures, yeast MO and the human state II MO-like complex may serve analogous roles by directly recruiting the second MCM hexamer to the first loaded MCM for double hexamer assembly. Thus, hereafter, we refer to the human complexes as MO.

MO-uncoupled MCM double hexamer assembly

Given our findings that (1) human ORC6 promotes robust MCM loading without MO state II and (2) both ORC6 and the ORC3 tether are dispensable for MCM double hexamer formation at higher ORC

and CDC6 concentrations, we considered the possibility of an alternative MCM loading mechanism. This rationale was reinforced by our observation that human MCM2–7 has a propensity to dimerize during protein purification, as demonstrated by its early elution in size-exclusion chromatograms (Extended Data Fig. 7a). Dimers can be seen both in negative-stain EM and in cryo-EM class averages, and they are structurally distinct from loaded MCM double hexamers (Extended Data Figs. 7b,c); we will thus refer to this double hexameric form of MCM2–7 as MCM dimer to distinguish it from the DNA-loaded double hexamer.

We determined the cryo-EM structure of this MCM dimer at a resolution of 3.8 Å, which was improved to 3.5 Å by symmetry expansion and local refinement (Extended Data Figs. 7d–h and 8a–e and Extended Data Table 1). In this structure, two MCM2–7 hexamers stack onto each other with the N-terminal domains facing (Fig. 5a). Both MCM2–7 rings adopt a left-handed lock-washer conformation with each of the MCM2/5 gates clearly open. This configuration restricts the dimerization interface to MCM3, MCM5 and MCM7, which engage the other hexamer using contacts that are similar to those in the loaded MCM double hexamer (Fig. 5b and Extended Data Fig. 8f–i). We observe clear density for nucleotide at five of the ATPase sites (all ATP except for ADP at the site of the interface between the MCM5 and MCM3 subunits (MCM5/MCM3)), whereas the sixth one (MCM2/5) is empty (Extended Data Fig. 6a,d). These structural features, in conjunction with the absence of DNA in the central pores, are consistent with MCM2–7 in the dimer being in a pre-loading state.

We next explored how MCM dimerization prior to loading might facilitate MCM double hexamer formation. We reasoned that the propensity of human MCM to dimerize might facilitate MCM double hexamer formation through an MO-independent or a non-canonical MO pathway, in which the second MCM is not directly recruited to the MO. There are several possibilities for how such a scenario could occur: first, MCM could be recruited and loaded onto DNA as a pre-formed dimer. Our data suggest that this event is infrequent. Although MCM dimerization is not affected by nucleotide or CDT1 addition, MCM dimers are temperature-sensitive at nanomolar protein concentrations (Extended Data Fig. 9a,b), and we rarely observed 2D class averages in which the ORC is bound to one of the hexamers in an MCM dimer (OCC–MCM dimer; Fig. 5c). Second, MCM2–7 could dimerize in the context of non-MO loading intermediates—that is, at the OCCM stage. Of note, we observe OCCM particles that appear to interact through the N-terminal face of MCM to form ‘double OCCMs’, especially at higher ORC and CDC6 concentrations (Fig. 5d). Third, MCM5, MCM3 and MCM7 (MCM5/MCM3/MCM7) co-association between hexamers could facilitate MCM double hexamer formation through sliding and dimerization of independently loaded MCM single hexamers, either bypassing the MO intermediate or as a result of ORC dissociation on DNA from MCM after MO formation but prior to second MCM hexamer recruitment. In contrast to OCC–MCM dimers and double OCCMs, DNA-loaded MCM single hexamers were observed in our cryo-EM data and were frequently seen in negative-stain class averages of loading reactions (Figs. 3d,e and 4a), leaving the possibility that they may encounter a second loaded hexamer through sliding. We therefore decided to test this third premise directly.

To determine whether human MCM double hexamers could form by dimerization of independently loaded hexamers, we developed a biochemical assay in which MCM single hexamers could be loaded onto DNA but not form double hexamers until after other loading factors had been removed (Fig. 5e). To prevent MCM dimerization, we added a maltose-binding protein (MBP) tag, followed by a TEV protease site, to the N terminus of MCM5, which is flexible in the MCM single hexamer but buried within the opposing hexamer in the MCM dimer and loaded double hexamer (Extended Data Fig. 9d). As expected, this complex purified as a single hexamer, was loaded onto DNA exclusively as single

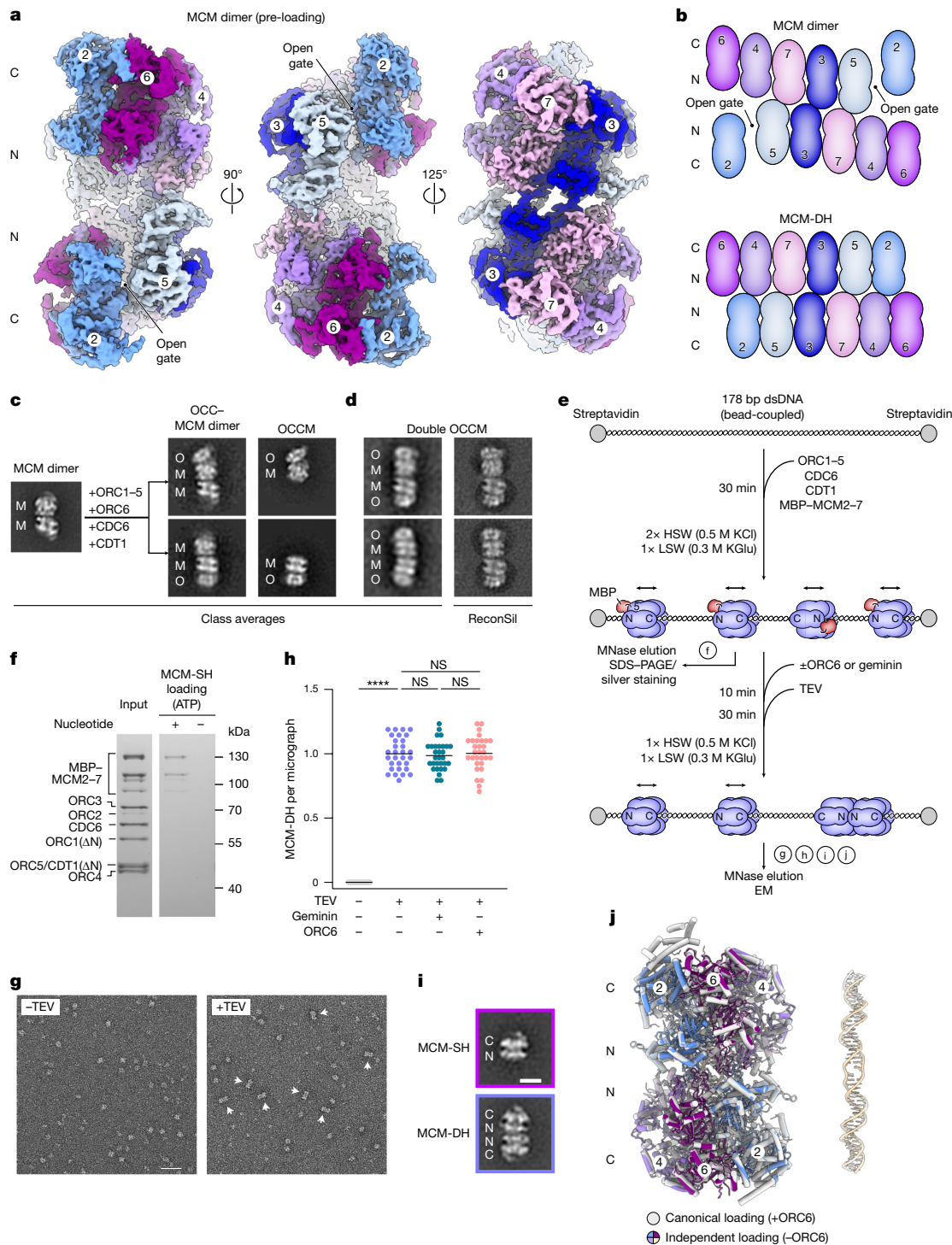


Fig. 5 | Human MCM2–7 hexamers can dimerize without other loading factors and mature into double hexamers by dimerization of independently loaded hexamers. **a**, Cryo-EM structure of the human MCM2–7 dimer. **b**, Schematic of subunit interactions in the MCM dimer and loaded MCM double hexamer. **c,d**, MCM dimers can associate with other loading factors. **c**, Negative-stain EM 2D class averages of a free MCM dimer, an ORC bound to one hexamer in MCM dimers (probably forming an ORC–CDC6–CDT1 (OCC)–MCM dimer complex), and of the canonical OCCM intermediate. Reactions were performed for 5 min with ATPγS without pre-heating MCM2–7. **d**, Class averages of double OCCMs and in silico reconstitution (ReconSil⁵) images of double OCCMs from reactions done with ATPγS. **e–j**, Independently loaded MCM single hexamers can dimerize on DNA to form double hexamers after removal of other loading factors. **e**, Overview of experimental setup. Letters in circles refer to results of respective experiments in **g–j**. **f**, Silver-stained SDS–PAGE of loading factor mix (input) and

loaded MCM single hexamers after removal of other loading factors. Solidus indicates that proteins migrate at the same position. **g**, Subregion of negative-stain electron micrograph of loaded MCM particles treated with or without TEV and eluted by MNase digestion. Double hexamers are marked with arrowheads. Scale bar, 50 nm. **h**, Quantification of MCM double hexamers per micrograph. Ten micrographs each in a total of three independent experiments per sample (total $n = 30$). Black lines represent means. Two-way ANOVA and Tukey's multiple comparison tests. *** $P < 0.0001$; NS, not significant. **i**, Two-dimensional class averages (from negative-stain EM) of MCM single and double hexamers after TEV cleavage as in **g,h**. Scale bar, 10 nm. **j**, Superposition of cryo-EM models of MCM-DHs loaded in canonical loading reactions and those formed by independent dimerization of single MCM hexamers on DNA. For gel source data, see Supplementary Information.

hexamers (0.5 M KCl wash) and did not form salt-stable double hexamers (1 M KCl wash; Extended Data Figs. 7a and 9c–g). Removing the MBP moiety by TEV digestion prior to loading restored salt-stable loading, indicating that the cleaved MCM hexamer is functional (Extended Data Fig. 9e–g).

We then loaded MBP-tagged single hexamers onto DNA without ORC6 to mitigate MO formation and washed away loading factors other than loaded MCM with 0.5 M KCl buffer (Fig. 5e,f and Extended Data Fig. 9h). If independently loaded single hexamers can dimerize, we should observe double hexamers in EM images of eluates after TEV addition. Indeed, TEV-treated but not mock-treated samples formed double hexamers (Fig. 5g–i). Inclusion of geminin or ORC6 during TEV cleavage did not alter the number of MCM-DHs observed, consistent with double hexamers not arising from new MCM loading or through MO formation (Fig. 5h). Similar to MCM-DHs loaded in canonical loading assays, double hexamers were salt-stable and MCM-SHs loaded with the full-length or IDR-deleted ORC and CDT1 matured into double hexamers with similar efficiency (Extended Data Fig. 9i–n). Cryo-EM analysis of MCM double hexamers assembled without ORC6 by dimerization of independently loaded single hexamers further revealed that they are structurally indistinguishable from MCM-DHs loaded in canonical loading reactions with ORC6 (Fig. 5j and Extended Data Fig. 10).

Collectively, these results demonstrate that human origin licensing can occur when recruitment and loading of the second MCM is uncoupled or independent of an MO intermediate and is mediated by dimerization of two independently loaded MCM2–7 complexes, probably after sliding on DNA. This mechanism can: (1) rationalize MCM loading by the MO state I intermediate incompatible with direct recruitment of a second MCM; and (2) partially explain the rescue of efficient MCM loading in the absence of ORC6 at higher ORC and CDC6 concentrations (Fig. 2e,f).

ORC6 disease variants impede MCM loading

Our observations of multiple routes towards human MCM double hexamer formation raises questions pertaining to their individual contributions to origin licensing in vivo. Mutations in ORC6 and other licensing factors are associated with a form of primordial dwarfism, Meier–Gorlin syndrome (MGS), that is caused by an impediment of DNA replication⁴⁴. We thus asked whether variants of ORC6 seen in individuals with MGS have a direct effect on MCM double hexamer formation in our in vitro MCM loading system, focusing on missense mutations in the CB-N region (K23E⁴⁵) and C-terminal domain (Y232S⁴⁶) of ORC6 (Fig. 6a and Extended Data Fig. 2d). Our results demonstrate that both ORC6 MGS mutants are defective in loading salt-stable MCM double hexamers without compromising MCM recruitment in bead-based loading assays (Fig. 6b,c). Moreover, negative-stain EM analyses of intermediates in MCM loading reactions (with ATP) showed a strong reduction in MO complex formation (Fig. 6d). These findings reinforce the conclusion that ORC6 is not strictly essential for human origin licensing, but that it increases MCM loading capacity through an MO-mediated loading pathway that is relevant to growth and cell proliferation at least during certain stages of development.

Discussion

Our findings favour the following model of human origin licensing pathways (Fig. 6f). The initiator ORC, with the help of CDC6 and CDT1, first recruits and loads a single MCM hexamer onto DNA through an OCCM intermediate, similarly to budding yeast^{14,47}. Human ORC6 is not required for this loading event (Figs. 2 and 4), in agreement with DNA-bound metazoan ORC structures that do not show ORC6 contributing to DNA binding and bending as in *S. cerevisiae* and with the absence or substoichiometry of ORC6 in human OCCM

structures^{12,29,48,49}. Our results further indicate that loaded human MCM single hexamers may then mature into double hexamers along several different routes: (1) a canonical MO-mediated mechanism; (2) a non-canonical MO-mediated mechanism; and (3) an MO-independent mechanism.

When ORC6 is available, MO-mediated pathways are likely to predominate (Fig. 6f(i),(ii)), in which ORC6 and ORC3 facilitate ORC binding to the N-terminal face of the first loaded MCM (Fig. 4). We postulate that the ORC is recruited from solution rather than through an ORC flip as seen in budding yeast, as human ORC6 has a weak affinity for ORC1–5 and lacks a sufficiently long linker for establishing a tether with the N-terminal surface of the MCM ring^{22–24} (Fig. 6e). The resultant human MO can exist in two different conformations (MO states I and II; Fig. 4). Only MO state II could accommodate the direct recruitment of a second MCM hexamer to the MO in a canonical, budding yeast-like MO pathway (Fig. 6f(i)). This canonical MO mechanism may arise either through direct formation of MO state II or through a shift between MO states I and II, possibly regulated by ORC6. The other conformation, MO state I, requires ORC6 to localize ORC1–5 to the first MCM hexamer and would be poised for second MCM recruitment only after conversion to state II or disengagement of the ORC from the first MCM, thereby uncoupling second MCM loading from the MO complex in a non-canonical MO pathway (Fig. 6f(ii)). In this regard, the interactions between MCM and ORC in the MO would serve to recruit and position the ORC on DNA in the correct direction for loading the second MCM hexamer, overcoming the need for specific DNA sequences to orient the ORC as in *S. cerevisiae*^{5,11,12,50}. Although the human MO pathways rationalize the enhanced MCM loading conferred by ORC6 in our biochemical system, they do not preclude other roles of ORC6 or of the human MO, such as stabilizing loaded MCM single hexamers or promoting MCM hexamer deposition through alternative mechanisms. The outcome of the human MO pathways would be analogous to MO-mediated MCM loading in *S. cerevisiae*, although the architecture of the MO, the role of ORC6, and the mechanisms used to achieve loading of an opposing second MCM have diverged from yeast to humans.

When ORC6 is not involved, MO formation is less efficient and MCM double hexamer assembly may arise through a combination of the canonical MO pathway (MO state II) and an MO-independent mechanism mediated by dimerization of independently loaded MCM hexamers (Fig. 6f(i),(iii)). The MO-independent pathway differs from MO-mediated pathways by the lack of an apparent mechanism to direct MCM orientation in the absence of sequence-specific origin recognition, suggesting that this pathway has a mere 25% chance for productive double hexamer formation. However, the MO-independent mechanism shares several notable similarities with the ORC6-mediated non-canonical MO pathway. Both mechanisms would require sliding of single MCM hexamers and/or OCCMs (or OCMs after CDC6 release) on DNA, properties that have been reported for the yeast intermediates^{50–52}. Moreover, dimerization of MCM into double hexamers would occur uncoupled from an MO, either bypassing this intermediate or after dissociation of MCM and ORC. Although our data support the conclusion that ORC6 stimulates MCM loading through MO formation, we cannot completely exclude the possibility that the MO is an off-pathway intermediate. In this regard, chromatin may aid in directing the orientation of MCM loading in an MO-independent pathway. Additionally, it is also possible that MO intermediates may inhibit MCM dimerization in some instances, as persistence of this complex would prevent productive MCM–MCM interactions in a double hexamer.

Given our data that ORC6-mediated MCM loading is more favourable, the question arises of why human cells, or metazoa more generally, would use multiple MCM loading mechanisms. Human cells depleted of ORC6 can sustain normal levels of MCM on chromatin (although it is unclear whether these MCMs are single or double

Article

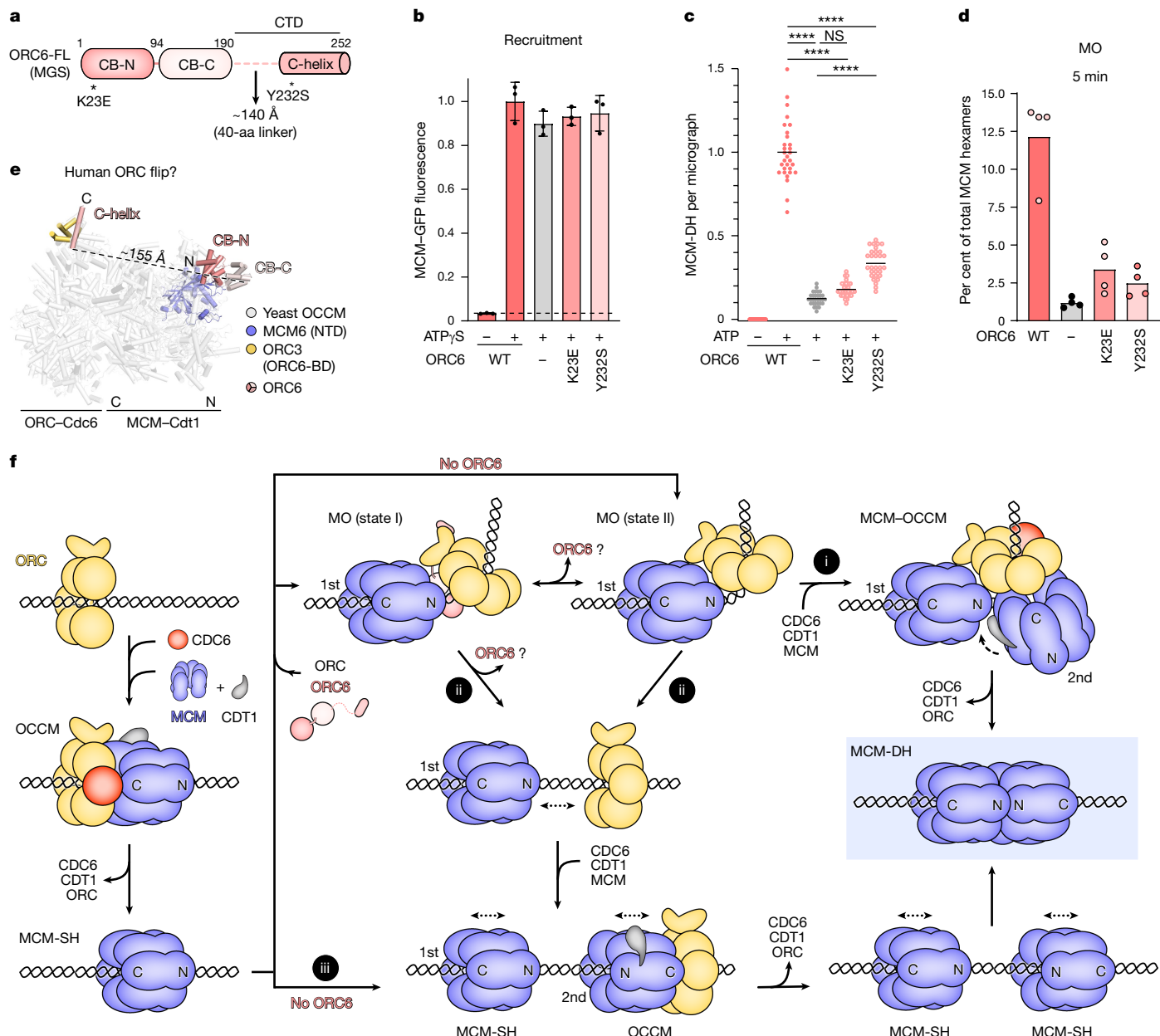


Fig. 6 | Disease-linked mutations in human ORC6 impair formation of the MO complex and MCM loading. **a**, Domain architecture of human ORC6, illustrating the location of mutations associated with MGS. A 40-amino-acid (approximately 140 Å long) linker connects the CB-C and C-terminal helix. **b**, MCM–GFP fluorescence in elutions of MCM recruitment reactions. Data are mean \pm s.d. of three independent experiments. The fluorescence signal was normalized to the average fluorescence signal obtained with wild-type ORC6. **c**, Quantification of MCM double hexamers observed in negative-stain electron micrographs of loading reaction elutions ($n = 30$ with 10 micrographs per each of 3 independent repeats). Two-way ANOVA and Tukey's multiple comparisons tests. Black lines represent means. *** $P < 0.0001$; NS, not significant. **d**, Quantification of MO particles by negative-stain EM and 2D classification of MCM loading reactions after 5 min of reaction time

(chosen because the MO intermediate is the most abundant at this time point; Extended Data Fig. 3g,h). Four independent experiments with 100–150 micrographs each were analysed per condition. **e**, Superposition of AlphaFold predictions of human ORC3–ORC6 and human MCM6–ORC6 onto the *S. cerevisiae* OCCM structure (PDB 5V8F¹⁵). The linker in human ORC6 is too short to span the shortest distance between the CB-C and C-terminal helix in ORC6 (approximately 155 Å) for an ORC flip. BD, binding domain. **f**, Model for human origin licensing pathways. (i) Canonical MO mechanisms; (ii) non-canonical MO mechanism; (iii) MO-independent mechanism. ORC6 is not depicted during OCCM assembly as it is not required for this MCM loading step and only weakly associates with the human ORC. We note that pathway (iii) could also occur by sliding of two OCCMs. Dotted arrows indicate sliding.

hexamers)³⁶, and some metazoa such as *Caenorhabditis elegans* do not have an ORC6 orthologue. These observations argue for an important role of ORC6-independent origin licensing. Nonetheless, ORC6 mutants associated with MGS are deficient in both MO and double hexamer formation (Fig. 6a-d), defects that are likely to be responsible for the reduced origin licensing capacity in cells of individuals

with MGS and lethality in flies^{53,54}, reinforcing the importance of ORC6-stimulated MCM loading. These seemingly disparate observations can be reconciled by our model and imply that not all MCM double hexamers may be loaded through the exact same mechanism in metazoan cells. Flexibility in MCM loading pathways would increase the chance of successful MCM double hexamer formation in

challenging cellular environments. The mechanism used to load an MCM double hexamer would probably depend on the local concentration of licensing factors at an origin at a given time, which may be substantially higher than those used in our reconstituted system due to liquid–liquid phase separation of loading factors^{30,31}. By contrast, budding yeast probably experiences evolutionary pressure to license most if not all of its origins by an Orc6- and MO-dependent mechanism to ensure efficient origin licensing control by CDK phosphorylation of Orc6 (and Orc2), which inhibits MO assembly and origin re-licensing in S phase^{19,55,56}. The diverged roles of Orc6 in budding yeast and metazoa are likely to reflect an evolutionary adaptation to both sequence-independent origin specification and reliance on ORC6- and MO-independent means to inhibit origin re-licensing in S phase in multicellular eukaryotes^{4,7}.

A second unexpected finding of our studies is the ability of human MCM2–7 to dimerize prior to loading (Fig. 5a,b). MCM self-association has been reported for endogenous human MCM2–7, but the nature of the complex formed has been unclear⁵⁷. Although there is currently no evidence to support that these MCM dimers can be directly loaded onto DNA, we speculate that the MCM5/MCM3/MCM7 inter-hexamer interface observed in the dimer may represent the initial contact during double hexamer formation. This interpretation is congruent with single-molecule studies in yeast showing that interactions between two MCM hexamers (involving Mcm7) are established before the loading of the second MCM, or Mcm2/5 gate closure, is completed^{18,58}. The propensity of MCMs to co-associate through MCM5/MCM3/MCM7 is likely to benefit the dimerization of MCM hexamers loaded in both MO-dependent and MO-independent manners, facilitating alignment of the correct inter-hexamer register.

In summary, our results suggest that human cells may use multiple pathways to license origins and provide key insights into how MCM loading mechanisms have diverged in multicellular eukaryotes. The plasticity of human origin licensing uncovered here may help to provide resilience against various cellular challenges and conditions, including replication stress and development programs. Moreover, this *in vitro* reconstitution system of human origin licensing represents a critical step towards future reconstitution of the entire replication initiation pathway in metazoan systems.

Online content

Any methods, additional references, Nature Portfolio reporting summaries, source data, extended data, supplementary information, acknowledgements, peer review information; details of author contributions and competing interests; and statements of data and code availability are available at <https://doi.org/10.1038/s41586-024-08237-8>.

- Bleichert, F. Mechanisms of replication origin licensing: a structural perspective. *Curr. Opin. Struct. Biol.* **59**, 195–204 (2019).
- Lewis, J. S. & Costa, A. Caught in the act: structural dynamics of replication origin activation and fork progression. *Biochem. Soc. Trans.* **48**, 1057–1066 (2020).
- Grewe, J. F., Zanetti, G., Miller, T. C. R. & Costa, A. In silico reconstitution of DNA replication: Lessons from single-molecule imaging and cryo-tomography applied to single-particle cryo-EM. *Curr. Opin. Struct. Biol.* **72**, 279–286 (2022).
- Costa, A. & Diffley, J. F. X. The initiation of eukaryotic DNA replication. *Annu. Rev. Biochem.* **91**, 107–131 (2022).
- Miller, T. C. R., Locke, J., Grewe, J. F., Diffley, J. F. X. & Costa, A. Mechanism of head-to-head MCM double-hexameric formation revealed by cryo-EM. *Nature* **575**, 704–710 (2019).
- Gupta, S., Friedman, L. J., Gelles, J. & Bell, S. P. A helicase-tethered ORC flip enables bidirectional helicase loading. *eLife* **10**, e74282 (2021).
- Parker, M. W., Botchan, M. R. & Berger, J. M. Mechanisms and regulation of DNA replication initiation in eukaryotes. *Crit. Rev. Biochem. Mol. Biol.* **52**, 107–144 (2017).
- Remus, D. et al. Concerted loading of Mcm2–7 double hexamers around DNA during DNA replication origin licensing. *Cell* **139**, 719–730 (2009).
- Ervin, C. et al. A double-hexameric MCM2–7 complex is loaded onto origin DNA during licensing of eukaryotic DNA replication. *Proc. Natl Acad. Sci. USA* **106**, 20240–20245 (2009).
- Gambus, A., Khoudoli, G. A., Jones, R. C. & Blow, J. J. MCM2–7 form double hexamers at licensed origins in *Xenopus* egg extract. *J. Biol. Chem.* **286**, 11855–11864 (2011).
- Bell, S. P. & Stillman, B. ATP-dependent recognition of eukaryotic origins of DNA replication by a multiprotein complex. *Nature* **357**, 128–134 (1992).
- Li, N. et al. Structure of the origin recognition complex bound to DNA replication origin. *Nature* **559**, 217–222 (2018).
- Speck, C., Chen, Z., Li, H. & Stillman, B. ATPase-dependent cooperative binding of ORC and Cdc6 to origin DNA. *Nat. Struct. Mol. Biol.* **12**, 965–971 (2005).
- Sun, J. et al. Cryo-EM structure of a helicase loading intermediate containing ORC–Cdc6–Cdt1–MCM2–7 bound to DNA. *Nat. Struct. Mol. Biol.* **20**, 944–951 (2013).
- Yuan, Z. et al. Structural basis of Mcm2–7 replicative helicase loading by ORC–Cdc6 and Cdt1. *Nat. Struct. Mol. Biol.* **24**, 316–324 (2017).
- Kang, S., Warner, M. D. & Bell, S. P. Multiple functions for Mcm2–7 ATPase motifs during replication initiation. *Mol. Cell* **55**, 655–665 (2014).
- Coster, G., Frigola, J., Beuron, F., Morris, E. P. & Diffley, J. F. Origin licensing requires ATP binding and hydrolysis by the MCM replicative helicase. *Mol. Cell* **55**, 666–677 (2014).
- Ticaud, S. et al. Mechanism and timing of Mcm2–7 ring closure during DNA replication origin licensing. *Nat. Struct. Mol. Biol.* **24**, 309–315 (2017).
- Amasino, A. L., Gupta, S., Friedman, L. J., Gelles, J. & Bell, S. P. Regulation of replication origin licensing by ORC phosphorylation reveals a two-step mechanism for Mcm2–7 ring closing. *Proc. Natl Acad. Sci. USA* **120**, e2221484120 (2023).
- Vashee, S. et al. Sequence-independent DNA binding and replication initiation by the human origin recognition complex. *Genes Dev.* **17**, 1894–1908 (2003).
- Remus, D., Beall, E. L. & Botchan, M. R. DNA topology, not DNA sequence, is a critical determinant for *Drosophila* ORC–DNA binding. *EMBO J.* **23**, 897–907 (2004).
- Dhar, S. K., Delmolino, L. & Dutta, A. Architecture of the human origin recognition complex. *J. Biol. Chem.* **276**, 29067–29071 (2001).
- Vashee, S., Simancik, P., Challberg, M. D. & Kelly, T. J. Assembly of the human origin recognition complex. *J. Biol. Chem.* **276**, 26666–26673 (2001).
- Bleichert, F. et al. A Meier–Gorlin syndrome mutation in a conserved C-terminal helix of Orc6 impedes origin recognition complex formation. *eLife* **2**, e00882 (2013).
- Gillespie, P. J., Li, A. & Blow, J. J. Reconstitution of licensed replication origins on *Xenopus* sperm nuclei using purified proteins. *BMC Biochem.* **2**, 15 (2001).
- Li, J. et al. The human pre-replication complex is an open complex. *Cell* **186**, 98–111 (2023).
- Noguchi, Y. et al. Cryo-EM structure of Mcm2–7 double hexamer on DNA suggests a lagging-strand DNA extrusion model. *Proc. Natl Acad. Sci. USA* **114**, E9529–E9538 (2017).
- Abid Ali, F. et al. Cryo-EM structure of a licensed DNA replication origin. *Nat. Commun.* **8**, 2241 (2017).
- Schmidt, J. M. & Bleichert, F. Structural mechanism for replication origin binding and remodeling by a metazoan origin recognition complex and its co-loader Cdc6. *Nat. Commun.* **11**, 4263 (2020).
- Parker, M. W. et al. A new class of disordered elements controls DNA replication through initiator self-assembly. *eLife* **8**, e48562 (2019).
- Hossain, M., Bhalla, K. & Stillman, B. Multiple, short protein binding motifs in ORC1 and CDC6 control the initiation of DNA replication. *Mol. Cell* **81**, 1951–1969 (2021).
- Wohlschlegel, J. A. et al. Inhibition of eukaryotic DNA replication by geminin binding to Cdt1. *Science* **290**, 2309–2312 (2000).
- Tada, S., Li, A., Maiorano, D., Mechali, M. & Blow, J. J. Repression of origin assembly in metaphase depends on inhibition of RLF-B/Cdt1 by geminin. *Nat. Cell Biol.* **3**, 107–113 (2001).
- Shibata, E. et al. Two subunits of human ORC are dispensable for DNA replication and proliferation. *eLife* **5**, e19084 (2016).
- Shibata, E. & Dutta, A. A human cancer cell line initiates DNA replication normally in the absence of ORC5 and ORC2 proteins. *J. Biol. Chem.* **295**, 16949–16959 (2020).
- Lin, Y. C. et al. Orc6 is a component of the replication fork and enables efficient mismatch repair. *Proc. Natl Acad. Sci. USA* **119**, e2121406119 (2022).
- Chou, H. C. et al. The human origin recognition complex is essential for pre-RC assembly, mitosis, and maintenance of nuclear structure. *eLife* **10**, e61797 (2021).
- Chen, S., de Vries, M. A. & Bell, S. P. Orc6 is required for dynamic recruitment of Cdt1 during repeated Mcm2–7 loading. *Genes Dev.* **21**, 2897–2907 (2007).
- Frigola, J., Remus, D., Mehanna, A. & Diffley, J. F. ATPase-dependent quality control of DNA replication origin licensing. *Nature* **495**, 339–343 (2013).
- Fernandez-Cid, A. et al. An ORC/Cdc6/MCM2–7 complex is formed in a multistep reaction to serve as a platform for MCM double-hexameric assembly. *Mol. Cell* **50**, 577–588 (2013).
- Wisniewski, J. R., Hein, M. Y., Cox, J. & Mann, M. A. “Proteomic ruler” for protein copy number and concentration estimation without spike-in standards. *Mol. Cell Proteomics* **13**, 3497–3506 (2014).
- Samel, S. A. et al. A unique DNA entry gate serves for regulated loading of the eukaryotic replicative helicase MCM2–7 onto DNA. *Genes Dev.* **28**, 1653–1666 (2014).
- Yuan, Z. et al. Structural mechanism of helicase loading onto replication origin DNA by ORC–Cdc6. *Proc. Natl Acad. Sci. USA* **117**, 17747–17756 (2020).
- Nielsen-Dandoroff, E., Ruegg, M. S. G. & Bicknell, L. S. The expanding genetic and clinical landscape associated with Meier–Gorlin syndrome. *Eur. J. Hum. Genet.* **31**, 859–868 (2023).
- Li, J. et al. A boy with Meier–Gorlin syndrome carrying a novel ORC6 mutation and uniparental disomy of chromosome 16. *Zhonghua Yi Xue Za Zhi* **34**, 68–72 (2017).
- Bicknell, L. S. et al. Mutations in the pre-replication complex cause Meier–Gorlin syndrome. *Nat. Genet.* **43**, 356–359 (2011).
- Ticaud, S., Friedman, L. J., Ivica, N. A., Gelles, J. & Bell, S. P. Single-molecule studies of origin licensing reveal mechanisms ensuring bidirectional helicase loading. *Cell* **161**, 513–525 (2015).
- Weissmann, F. et al. MCM double hexamer loading visualised with human proteins. Preprint at bioRxiv <https://doi.org/10.1101/2024.04.10.588848> (2024).
- Wells, J. N. et al. Reconstitution of human DNA licensing and the structural and functional analysis of key intermediates. Preprint at bioRxiv <https://doi.org/10.1101/2024.04.11.589023> (2024).

Article

50. Coster, G. & Diffley, J. F. X. Bidirectional eukaryotic DNA replication is established by quasi-symmetrical helicase loading. *Science* **357**, 314–318 (2017).
51. Sanchez, H. et al. DNA replication origins retain mobile licensing proteins. *Nat. Commun.* **12**, 1908 (2021).
52. Zhang, A., Friedman, L. J., Gelles, J. & Bell, S. P. Changing protein-DNA interactions promote ORC binding-site exchange during replication origin licensing. *Proc. Natl Acad. Sci. USA* **120**, e2305556120 (2023).
53. Stiff, T. et al. Deficiency in origin licensing proteins impairs cilia formation: implications for the aetiology of Meier–Gorlin syndrome. *PLoS Genet.* **9**, e1003360 (2013).
54. Balasov, M., Akhmetova, K. & Chesnokov, I. Drosophila model of Meier–Gorlin syndrome based on the mutation in a conserved C-terminal domain of Orc6. *Am. J. Med. Genet. A* **167A**, 2533–2540 (2015).
55. Nguyen, V. Q., Co, C. & Li, J. J. Cyclin-dependent kinases prevent DNA re-replication through multiple mechanisms. *Nature* **411**, 1068–1073 (2001).
56. Lim, C. T. et al. Cell cycle regulation has shaped budding yeast replication origin structure and function. Preprint at *bioRxiv* <https://doi.org/10.1101/2024.01.10.575016> (2024).
57. Xu, N. et al. Cryo-EM structure of human hexameric MCM2–7 complex. *iScience* **25**, 104976 (2022).
58. Champasa, K., Blank, C., Friedman, L. J., Gelles, J. & Bell, S. P. A conserved Mcm4 motif is required for Mcm2–7 double-hexameric formation and origin DNA unwinding. *eLife* **8**, e45538 (2019).

Publisher's note Springer Nature remains neutral with regard to jurisdictional claims in published maps and institutional affiliations.

Springer Nature or its licensor (e.g. a society or other partner) holds exclusive rights to this article under a publishing agreement with the author(s) or other rightsholder(s); author self-archiving of the accepted manuscript version of this article is solely governed by the terms of such publishing agreement and applicable law.

© The Author(s), under exclusive licence to Springer Nature Limited 2024

Methods

Protein constructs and baculovirus generation

Full-length and truncated *Homo sapiens* (*Hs*) ORC1–5 (Uniprot identifiers: Q13415 for ORC1, Q13416 for ORC2, Q9UBD5 for ORC3, O43929 for ORC4 (natural variant N78S), O43913 for ORC5) were reconstituted in insect cells by infection with baculoviruses expressing multiple ORC subunits. To generate ORC-containing baculovirus vectors, full-length ORC subunits or N-terminally truncated ORC1 (amino acids 400–861, referred to as ORC1(ΔN)) were first cloned into a ligation-independent-cloning (LIC)-compatible pFastBac vector⁵⁹ (Macrolab, University of California Berkeley, USA). For purification, a hexa-histidine (6×His) tag and a MBP tag, both followed by a tobacco etch virus (TEV) protease cleavage site, were added to the N termini of ORC1 and ORC4, respectively. For expression of *Hs*ORC2–5, the 6×His–TEV tag was moved to the N terminus of ORC2. ORC3(ΔT) (deletion of amino acid residues 517–544) was generated by mutagenesis and verified by DNA sequencing. Subsequently, ORC subunits were combined into a pFastBac-derived BioBricks MultiBac vector (Macrolab) by subcloning different combinations of *Hs*ORC1–5 genes⁵⁹. Bacmids were generated in DH10Bac cells and used for transfections of Sf9 cells (Thermo Fisher Scientific) with Cellfectin II (Thermo Scientific Fisher). Baculoviruses were amplified for two rounds in Sf9 cells to obtain high-titre viruses for infection of Hi5 cells for large-scale expression.

Full-length wild-type (amino acids 1–252), MGS-mutant (K23E and Y232S) and truncated (CB-N: amino acids 1–94, ΔCTD: amino acids 1–190, CB-C: amino acids 95–190, and ΔCB-N: amino acids 95–252) *Hs*ORC6 (Uniprot identifier Q9Y5N6) were cloned as N-terminal 6×His–TEV fusions into a LIC-converted, pET-derived *Escherichia coli* expression vector (Macrolab). The full-length construct was used as a template to generate expression vectors encoding ORC6 MGS mutants (ORC6(K23E) and ORC6(Y232S)) by site-directed mutagenesis. Mutations were verified by DNA sequencing.

*Hs*CDC6 (Uniprot identifier Q99741) was expressed in insect cells. The coding sequences of full-length or N-terminally truncated CDC6 (CDC6(ΔN), amino acids 134–560) were cloned into the LIC-compatible pFastBac vector (Macrolab) with an N-terminal 6×His–MBP tag and a TEV cleavage site. Bacmid generation and baculovirus amplification were performed as described for *Hs*ORC1–5.

Full-length human CDT1 (Uniprot identifier Q9H211) was expressed in insect cells, while truncated *Hs*CDT1 was expressed in *E. coli*. The coding sequence of full-length CDT1 was cloned into the LIC-compatible pFastBac vector (Macrolab) with an N-terminal 6×His–MBP tag and a TEV cleavage site. Bacmid generation and baculovirus amplification were performed as described for *Hs*ORC1–5. The coding sequence of truncated CDT1 (CDT1(ΔN), amino acids 167–546) was cloned as N-terminal 6×His–TEV fusion into a LIC-converted, pET-derived *E. coli* expression vector (Macrolab).

*Hs*MCM2–7 (Uniprot identifiers: P49736 for MCM2, P25205 for MCM3, P33991 for MCM4 (natural variant L650M), P33992 for MCM5, Q14566 for MCM6, P33993 for MCM7) was reconstituted in insect cells. MCM2–7 subunits were cloned into two pFastBac-derived BioBricks MultiBac expression vectors⁵⁹, one construct containing MCM2 (with or without a C-terminal msfGFP tag), MCM4, and MCM6, and the other MCM3, MCM5, and MCM7. For affinity purification, MCM3 and MCM4, or MCM5 and MCM7, were tagged N-terminally with MBP and 6×His, respectively, each followed by a TEV protease cleavage site.

Full-length *Hs*Geminin (Uniprot identifier O75496) was cloned into a LIC-converted, pET-derived vector for expression in *E. coli* with an N-terminal 6×His–TEV tag.

Expression and purification of the recombinant *Hs*ORC

Full-length or ORC1-truncated *Hs*ORC1–5, a *Hs*ORC with ORC3(ΔT), and *Hs*ORC2–5 were purified at 4 °C from Hi5 cells (Thermo Scientific Fisher) infected with baculoviruses expressing a combination of single

or multiple *Hs*ORC subunits. After 48 h infection, Hi5 cells were collected and resuspended in 35 ml lysis buffer (50 mM Tris-HCl (pH 7.8), 300 mM KCl, 50 mM imidazole, 10% glycerol, 200 μM PMSF, 1 μg ml⁻¹ leupeptin, 1 mM β-mercaptoethanol (β-ME)) per litre culture. The cell suspension was sonicated and the lysate clarified by ultracentrifugation at 142,032g for 45 min in a Beckman Coulter Optima L-80 XP ultracentrifuge. The soluble fraction was subjected to ammonium sulfate precipitation (final 20% (v/v)) and subsequently cleared once more by ultracentrifugation. The supernatant was loaded onto a 5 ml HisTrap HP Nickel-affinity chromatography column (Cytiva) that was washed with 60 ml lysis buffer prior to *Hs*ORC elution with a 50–250 mM imidazole gradient. Peak fractions were further purified on 7.5–10 ml amylose columns (New England Biolabs) in 50 mM Tris-HCl (pH 7.8), 300 mM KCl, 10% glycerol, 1 mM β-ME and eluted with 20 mM maltose. The *Hs*ORC was incubated with 6×His-tagged TEV protease overnight, which was removed by nickel-affinity chromatography using a 5 ml HisTrap HP column (Cytiva, equilibrated in 50 mM Tris-HCl (pH 7.8), 300 mM KCl, 10% glycerol, 50 mM imidazole, 1 mM β-ME). The flow-through was concentrated and loaded onto HiPrep 16/60 Sephacryl S-400 HR or Superose 6 Increase 10/300 GL columns (Cytiva) equilibrated in 25 mM HEPES-KOH (pH 7.6), 500 mM potassium glutamate, 10% glycerol, 1 mM DTT. *Hs*ORC peak fractions were pooled and concentrated in 30 K Amicon Ultra-15 concentrators (Millipore), aliquoted, and flash-frozen in liquid nitrogen for storage at –80 °C.

Expression and purification of recombinant *Hs*ORC6

All ORC6 constructs were expressed in BL21 RIL *E. coli* cells. Two litres of shaker culture in 2×YT medium with 30 μg ml⁻¹ kanamycin and 34 μg ml⁻¹ chloramphenicol were grown at 37 °C to an OD_{600 nm} of 0.5–0.6. For ORC6 mutants, the medium was supplemented with 2% glucose. Expression was induced with 0.5 mM isopropyl β-D-1-thiogalactopyranoside (IPTG) for about 18 h at 16 °C. Cells were collected by centrifugation and lysed by sonication in 50 ml lysis buffer containing 50 mM Tris-HCl (pH 8.0), 800 mM KCl, 10% glycerol, 30 mM imidazole, 1 mM β-ME, 200 μM PMSF, and 1 μg ml⁻¹ leupeptin. The lysate was clarified by centrifugation at 23,426g for 35 min and loaded on a 5 ml HisTrap HP column (Cytiva). After a wash with 200 ml lysis buffer, ORC6 was eluted with 50 mM Tris-HCl (pH 8.0), 150 mM KCl, 250 mM imidazole, 10% glycerol, 1 mM β-ME. The 6×His tag was cleaved by digestion with 6×His-tagged TEV protease during overnight dialysis into 50 mM Tris-HCl (pH 8.0), 150 mM KCl, 10% glycerol, 30 mM imidazole, and 1 mM β-ME. TEV protease and uncleaved ORC6 were removed by passing the protein solution over a 5 ml HisTrap HP column (Cytiva) equilibrated in dialysis buffer. Subsequently, cleaved ORC6 was further purified by gel filtration chromatography on a HiLoad 16/60 Superdex 75 pg column (Cytiva) equilibrated in 50 mM Tris-HCl (pH 8.0), 150 mM KCl, 10% glycerol, 1 mM DTT. Peak fractions were pooled, concentrated, aliquoted, and flash-frozen in liquid nitrogen for storage at –80 °C.

Expression and purification of recombinant *Hs*CDC6

Full-length *Hs*CDC6 was purified at 4 °C from Hi5 cells. After 48 h infection with baculovirus, Hi5 cells were collected, resuspended in 35 ml lysis buffer (50 mM Tris-HCl (pH 7.8), 300 mM KCl, 30–50 mM imidazole, 10% glycerol, 200 μM PMSF, 1 μg ml⁻¹ leupeptin, 1 mM β-ME) per litre culture, and sonicated. The lysate was then clarified by two rounds of ultracentrifugation and ammonium sulfate precipitation as described previously for the *Hs*ORC. The supernatant was loaded onto a 5 ml HisTrap HP Nickel-affinity chromatography column (Cytiva) that was washed with 60 ml lysis buffer prior to elution with 250 mM imidazole. The protein was further purified on a 5–10 ml amylose column (New England Biolabs) in 50 mM Tris-HCl (pH 7.8), 300 mM KCl, 10% glycerol, 1 mM β-ME and eluted with 20 mM maltose. The *Hs*CDC6 elution was concentrated in a 30 K Amicon Ultra-15 concentrator (Millipore) and loaded onto a HiLoad 16/600 Superdex 200 pg column (Cytiva) equilibrated in 50 mM Tris-HCl (pH 7.8), 300 mM KCl, 10%

Article

glycerol, 1 mM DTT. Peak fractions were incubated with 6×His-tagged TEV protease overnight and then purified over another 5 ml HisTrap HP column (Cytiva) equilibrated in 50 mM Tris-HCl (pH 7.8), 300 mM KCl, 10% glycerol, 50 mM imidazole, 1 mM β-ME to remove TEV, uncleaved CDC6, and 6×His-MBP (this step was omitted for purification of 6×His-MBP–CDC6). A final gel filtration chromatography step was performed using a HiLoad 16/600 Superdex 200 pg column (Cytiva). Afterwards, HsCDC6 peak fractions were pooled, concentrated, aliquoted, and flash-frozen in liquid nitrogen for storage at –80 °C. Truncated HsCDC6 was purified similarly to the full-length protein except that the amylose affinity step was omitted.

Expression and purification of recombinant HsCDT1

Full-length HsCDT1 was expressed and purified at 4 °C from Hi5 cells infected with baculovirus for 48 h. Cells were collected and resuspended in 60 ml lysis buffer (50 mM Tris-HCl (pH 7.8), 1 M NaCl, 10% glycerol, 30 mM imidazole, 5 mM β-ME, 200 μM PMSF, 1 μg ml⁻¹ leupeptin) per litre culture. After sonication, the lysate was clarified by two rounds of ultracentrifugation and ammonium sulfate precipitation as described for the HsORC. The supernatant was loaded onto a 5 ml HisTrap HP Nickel-affinity chromatography column (Cytiva) that was washed with 200 ml lysis buffer and 50 ml low-salt buffer (50 mM Tris-HCl (pH 7.8), 300 mM KCl, 10% glycerol, 30 mM imidazole, 5 mM β-ME), eluted onto a 5 ml HiTrap Q HP ion exchange column (Cytiva) with 250 mM imidazole in 50 mM Tris-HCl (pH 7.8), 300 mM KCl, 10% glycerol, 5 mM β-ME. Fractions containing CDT1 were further purified on a 5 ml amylose column (New England Biolabs) in 50 mM Tris-HCl (pH 7.8), 300 mM KCl, 10% glycerol, 5 mM β-ME and eluted with 20 mM maltose. The 6×His-MBP-tag was cleaved off by addition of 6×His-tagged TEV protease overnight, after which TEV was removed using a HisTrap HP column (Cytiva). The flow-through was concentrated and loaded onto a HiLoad 16/600 Superdex 200 pg column (Cytiva) equilibrated in 50 mM Tris-HCl (pH 7.8), 150 mM KCl, 10% glycerol, 1 mM DTT. HsCDT1 peak fractions were pooled and concentrated in a 30 K Amicon Ultra-15 concentrator (Millipore), aliquoted, and flash-frozen in liquid nitrogen for storage at –80 °C.

Truncated HsCDT1 (amino acids 167–546) was expressed in BL21 RIL *E. coli* cells grown in 2×YT medium with 30 μg ml⁻¹ kanamycin and 34 μg ml⁻¹ chloramphenicol. Expression was induced at an OD_{600 nm} of 0.5–0.6 with 0.5 mM IPTG overnight at 16 °C. Cells were collected by centrifugation and resuspended in about 20 ml lysis buffer (50 mM Tris-HCl (pH 7.8), 1 M NaCl, 10% glycerol, 30 mM imidazole, 5 mM β-ME, 200 μM PMSF, 1 μg ml⁻¹ leupeptin) per litre culture. The cell suspension was sonicated and the lysate was clarified by centrifugation at 23,426g in a Sorvall Evolution RC Superspeed centrifuge (Thermo Fisher Scientific). CDT1(ΔN) was purified by nickel-affinity and ion exchange chromatography as described for the full-length protein. Subsequently, the affinity tag was removed by digestion with 6×His-tagged TEV protease overnight during dialysis into 50 mM Tris-HCl (pH 7.8), 300 mM KCl, 10% glycerol, 5 mM β-ME, followed by nickel-affinity chromatography to remove TEV and uncleaved CDT1. The flow-through was concentrated and loaded onto a HiLoad 16/600 Superdex 200 pg column (Cytiva) equilibrated in 50 mM Tris-HCl (pH 7.8), 150 mM KCl, 10% glycerol, 1 mM DTT. HsCDT1(ΔN) peak fractions were pooled and concentrated in a 30 K Amicon Ultra-15 concentrator (Millipore), aliquoted, and flash-frozen in liquid nitrogen for storage at –80 °C.

Expression and purification of recombinant HsMCM2-7

HsMCM2-7 (containing untagged MCM2 or C-terminally msfGFP-tagged MCM2) were purified at 4 °C from Hi5 cells co-infected with baculoviruses expressing HsMCM2–MCM4–MCM6 and HsMCM3–MCM5–MCM7 subunits. Cells were collected by centrifugation and resuspended in 35 ml lysis buffer (50 mM HEPES-KOH (pH 7.5), 300 mM potassium acetate, 10% glycerol, 30 mM imidazole, 1 mM β-ME, 1 μg ml⁻¹ leupeptin, 200 μM PMSF) per litre culture. After sonication, the lysate

was clarified by two rounds of ultracentrifugation and ammonium sulfate precipitation as described for the HsORC. HsMCM2-7 was purified using a 5 ml HisTrap HP column (Cytiva) and eluted using 250 mM imidazole in 50 mM HEPES-KOH (pH 7.5), 200 mM potassium acetate, 10% glycerol, 1 mM β-ME. Eluted proteins were loaded onto a 6 ml amylose column (New England Biolabs), washed in 50 mM HEPES-KOH (pH 7.5), 300 mM potassium acetate, 10% glycerol, 1 mM β-ME, and MCM2-7 was eluted with 20 mM maltose in wash buffer. Affinity tags were removed by digestion with 6×His-tagged TEV protease and passing the protein solution over another 5 ml HisTrap HP column (Cytiva) equilibrated in 50 mM HEPES-KOH (pH 7.5), 200 mM potassium acetate, 30 mM imidazole, 10% glycerol, 1 mM β-ME. The flow-through was concentrated and loaded onto a Superose 6 Increase 10/300 GL column (Cytiva) in 25 mM HEPES-KOH (pH 7.5), 300 mM potassium acetate, 10% glycerol, 1 mM DTT. HsMCM2-7 peak fractions were pooled, concentrated, and flash-frozen in liquid nitrogen for storage at –80 °C. For purification of MBP–MCM2-7 (with MBP on MCM5), the TEV cleavage step was omitted and the complex directly loaded onto a Superose 6 column after amylose affinity chromatography.

Expression and purification of recombinant HsGeminin

HsGeminin was expressed in *E. coli* BL21 RIL cells overnight at 16 °C upon induction with 0.5 mM IPTG at an OD_{600 nm} of 0.5. Cells were collected, resuspended in 25 ml lysis buffer per litre culture (50 mM Tris-HCl (pH 7.8), 800 mM KCl, 50 mM imidazole, 10% glycerol, 1 mM β-ME, 1 μg ml⁻¹ leupeptin, 200 μM PMSF), and lysed by sonication. The clarified lysate was used to purify HsGeminin by nickel-affinity chromatography on a 5 ml HisTrap HP column (Cytiva), which was washed with 350 ml lysis buffer. HsGeminin was eluted with 50 mM Tris-HCl (pH 7.8), 600 mM KCl, 250 mM imidazole, 10% glycerol, 1 mM β-ME. After concentration of the eluate, the protein was further purified by size-exclusion chromatography in 50 mM Tris-HCl (pH 7.8), 300 mM KCl, 10% glycerol, 1 mM DTT using a HiLoad 16/600 Superdex 200 pg column (Cytiva). Protein in peak fractions was concentrated, flash-frozen, and stored at –80 °C.

MCM2-7 loading assay

In vitro MCM2-7 loading assays using human proteins were adapted from those established previously for the *Drosophila* system²⁹. First, 2.4 pmol of 178 bp biotinylated duplex²⁹ were coupled to 10 μl streptavidin sepharose high performance beads (Cytiva) in ~20 μl coupling buffer (5 mM Tris-HCl (pH 8.0), 0.5 mM EDTA, 1 M NaCl, 0.01% NP-40) for 30 min. The beads were washed with coupling buffer and 2.4 pmol streptavidin (Sigma Aldrich) were added for 15 min to block any free DNA ends. Subsequently, beads were washed thrice in low-salt buffer (25 mM HEPES-KOH (pH 7.6), 300 mM potassium glutamate, 10 mM magnesium acetate, 10% glycerol, 0.01% NP-40, 1 mM DTT). The full-length or truncated ORC, CDC6, CDT1 and MCM2-7 were mixed at 60 nM, 60 nM, 120 nM and 120 nM, respectively, as the standard final concentration in low-salt buffer with or without 1 mM ATP or ATP^yS. In assays with Geminin, the ORC, CDC6, CDT1 and MCM2-7 were mixed with Geminin prior to addition to DNA-bound beads. Forty microlitres of the protein mix were added to DNA-coupled beads and incubated for 30 min at 37 °C. To assess MCM2-7 loading, beads were washed once with high-salt buffer (25 mM HEPES-KOH (pH 7.6), 1 M KCl, 10 mM magnesium acetate, 10% glycerol, 0.01% NP-40, 1 mM DTT) with 0 or 1 mM ATP, followed by two washes with low-salt buffer with 0 or 1 mM ATP. To assess MCM2-7 recruitment, beads were washed thrice with low-salt buffer. Bound proteins were eluted by digestion with 500 units micrococcal nuclease (New England Biolabs) for 10 min at 37 °C in 25 mM HEPES-KOH (pH 7.6), 300 mM KCl, 10 mM magnesium acetate, 10% glycerol, 0.01% NP-40, 5 mM CaCl₂, 1 mM DTT, 0 or 1 mM ATP (for loading) or 1 mM ATP^yS (for recruitment), and analysed by SDS-PAGE and silver staining. All loading assays were performed at minimum as three independent experiments. For quantification of

Geminin titrations, the band intensity of MCM2 was measured in ImageJ and normalized to the MCM2 intensity from recruitment or loading reactions done without Geminin for each experiment. Generally, all assays were performed with truncated ORC1 and CDT1 but full-length CDC6 unless stated otherwise.

Fluorescence-based MCM2–7 loading assays were performed similarly with the following modifications. Three pmol of biotinylated DNA were coupled to 10 µl Dynabeads MyOne Streptavidin T1 (Thermo Fisher Scientific) and free ends were blocked with 3 pmol streptavidin afterwards. MCM2–7 recruitment and loading reactions were performed at 37 °C for 40 min in 40 µl each containing 60 nM ORC1–5 (with ORC1(ΔN)), 60 nM CDC6, 120 nM CDT1(ΔN), and 120 nM GFP–MCM2–7. Beads were washed once each with high-salt wash and low-salt wash buffer for loading reactions, and twice with low-salt wash buffer for recruitment reactions. MNase elutions were transferred to a 384-well plate and GFP fluorescence in eluates measured in a PHERAstar FSX plate reader (BMG Labtech) with excitation at 485 nm and emission at 520 nm using a gain setting of 700. Fluorescence intensities from at least three independent experiments were normalized to the average GFP signal from recruitment or loading reactions done with wild-type proteins. For ORC/CDC6 titrations, ORC1–5 (ORC1(ΔN)), ORC6 and CDC6 concentrations of 30, 60, 120, 240 and 480 nM were used, while GFP–MCM2–7 and CDT1(ΔN) were kept constant at 120 nM. GFP fluorescence in eluates was measured with a gain setting of 500 and 700 for recruitment and loading, respectively. Background fluorescence was accounted for by subtracting the fluorescence intensity measured from a reaction without ATP or ATP γ S. Relative MCM2–7 loading efficiencies were calculated by dividing the measured GFP fluorescence intensities in eluates of reactions without ORC6 by those with ORC6 for at least three independent replicate experiments.

To assess dimerization of independently loaded MCM hexamers, MCM was first loaded onto bead-coupled DNA (using streptavidin sepharose high performance beads (Cytiva)) in 40 µl reactions containing 120 nM of ORC1–5 (full-length or truncated ORC1), CDC6, CDT1 (full-length or truncated), and MBP–MCM2–7 (MBP–MCM5) for 30 min at 37 °C. Due to the lower stability of loaded single hexamers, beads were washed twice with a modified high-salt buffer using 0.5 M KCl instead of 1 M KCl, and once with low-salt buffer (with 1 mM ATP). Beads were then resuspended in 40 µl low-salt buffer (with 1 mM ATP) without or with (when indicated) 120 nM ORC6 or 600 nM Geminin and incubated for 10 min at 30 °C. Subsequently, TEV protease was added to a final concentration of 2.5 µM, and reactions were incubated for 30 min at 30 °C and another 10 min at 37 °C. Beads were washed with high-salt (0.5 M KCl or 1 M KCl) and low-salt buffer with 1 mM ATP. MCM2–7 was eluted by MNase digestion as described above and 4 µl of the elution were used to prepare negative-stain EM grids (see below). Functionality of cleaved MCM2–7 purified with MBP–MCM5 was confirmed in standard loading assays by pre-treating MCM2–7 with 5 µM TEV for 30 min at 30 °C.

Negative-stain EM

Samples for negative staining were prepared as described below, applied to glow-discharged, continuous carbon EM grids (Ted Pella), and stained with 2% uranyl acetate. EM grids were imaged in a Talos L120C transmission electron microscope operated at 120 kV. Micrographs were either collected manually or automatically using SerialEM⁶⁰ at magnifications of 36,000 \times , 45,000 \times or 73,000 \times .

MCM2–7 loading reaction eluates. To analyse the outcome of bead-based MCM2–7 loading assays by negative-stain EM, 4 µl of proteins eluted from streptavidin beads were applied to glow-discharged continuous carbon grids for 1 min (or 5 min for MCM dimerization assays from loaded single hexamers) and stained by incubating the grids on 3 \times 40 µl drops of 2% uranyl acetate for 10 s each, followed by a final 30-second incubation before blotting away the excess uranyl acetate.

For quantification, MCM2–7 double hexamer particles per electron micrograph were counted manually, with all micrographs in a given experiment collected at the same magnification so that MCM-DH particles are counted on the same total area of an EM grid. A total of at least three independent replicate experiments were done for each experimental condition, with a minimum of ten micrographs recorded and analysed per replicate. The data were normalized to the average number of MCM2–7 double hexamers per electron micrograph observed in reactions containing all loading factors (full-length or wild-type proteins). Statistical significance was calculated using two-way ANOVA with Tukey post-hoc analysis in GraphPad Prism.

MCM2–7 loading intermediates. ORC1–5 (ORC1(ΔN)), CDC6, CDT1(ΔN) and MCM2–7 were mixed at 120 nM each with 180 nM biotinylated DNA and 360 nM streptavidin, either with or without 120 nM ORC6, in low-salt buffer (25 mM HEPES-KOH (pH 7.6), 300 mM potassium glutamate, 10 mM magnesium acetate, 10% glycerol, 0.01% NP-40, 1 mM DTT, 1 mM ATP or ATP γ S). To simplify interpretation of intermediates, MCM2–7 was incubated at 37 °C for 20 min prior to assembling loading reactions to dissociate MCM2–7 dimers. Loading reactions were incubated at 37 °C for 30 min (or shorter for time-course experiments), placed on ice for 10 s, and then 4 µl were immediately applied to EM grids. After a 10-s incubation, EM grids were stained on three 40 µl drops of 2% uranyl acetate for 10 s each, followed by a final incubation for 30 s, after which the remaining stain was gently blotted away. EM grid areas with appropriate stain thickness were chosen for data collection. Typically, two or more datasets from independently prepared loading reactions were collected for each condition at 45,000 \times magnification, with approximately 150 micrographs for each dataset. Particles were picked automatically (reference-free) using GAUTOMATCH (K. Zhang, MRC-LMB, Cambridge), extracted from phase-flipped micrographs (done using GCTF⁶¹), and subjected to 2D classification in RELION 4.0.1⁶². The relative abundance of different MCM-containing complexes was calculated based on particle numbers in well-defined 2D classes as a fraction (or per cent) of the total number of MCM-containing particles. Time points in time-course experiments refer to the beginning of the loading reaction until the end of 37 °C incubation; EM grids were prepared at room temperature, at which MCM loading is inefficient.

For structural analysis of MO intermediates, MO-like particles from multiple datasets were combined and used for ab initio reconstruction in CryoSPARC v4.2.1⁶³. Two classes were identified that contained clear density for an MCM hexamer but differed in the orientation of the ORC. Both volumes were refined using one round of heterogeneous and homogeneous refinement in CryoSPARC. Docking of MCM-SH (this study), a single hexamer from the loaded MCM-DH (PDB 7W1Y²⁶), and the ORC (PDB 7JP0⁶⁴) into the EM maps was done using UCSF Chimera^{65,66}. The orientation of MCM2–7 was determined using the winged helix domains of MCM2, MCM5, and MCM6 as reference point because they interact and form a prominent map region at the C-terminal side of the MCM2–7 ring²⁶. Two-dimensional projections for comparison with 2D class averages were generated by converting model coordinates into maps and low-pass filtering volumes to 25 Å.

Purified HsMCM2–7 (pre-loading state). Purified recombinant MCM2–7 was diluted to 80 nM in 25 mM HEPES-KOH (pH 7.5), 10 mM magnesium acetate, 0.3 M potassium glutamate, 10% glycerol, 1 mM DTT, either in the absence or presence of 1 mM ATP and/or 240 nM full-length CDT1 (final concentration). Four µl of each sample were applied to EM grids prior to staining. Equilibrium studies were performed at 2 µM MCM2–7 and the complex was diluted to 80 nM prior to EM grid preparation.

Cryo-EM of MCM2–7 loading reactions

Cryo-EM sample preparation and data collection. Truncated ORC1–5 (ORC1(ΔN)), ORC6, 6 \times His–MBP–CDC6 and a 480-bp dsDNA fragment

Article

(obtained by PCR of the *S. cerevisiae* ARS1 locus with oligos 5'-GG ACTGACGCCAGAAATGTTG-3' and 5'-CGAGGATACGGAGAGAGGTATG-3') were mixed at 100 nM concentration with 200 nM truncated CDT1 and MCM2-7 in 25 mM HEPES-KOH (pH 7.6), 10 mM magnesium acetate, 0.3 M potassium glutamate, 1 mM DTT, and 1 mM ATP. MCM2-7 was preincubated at 37 °C for 20 min to disassemble MCM2-7 dimers prior to mixing with the other proteins. After a 5-min incubation at 37 °C, 3.5 µl of this protein-DNA mix were applied to 300-mesh copper R2/1 Quantifoil Holey Carbon Grids (Quantifoil Micro Tools) that had been freshly glow-discharged for 30 s at 25 mA in a GloQube Plus Glow Discharge System (Quorum Technologies) and treated with graphene oxide (Sigma Aldrich) as described previously⁶⁷. Grids were blotted for 4 s and vitrified in liquid ethane using a Vitrobot Mark IV plunge freezer (Thermo Fisher Scientific). Cryo-EM grids were pre-screened in a 200 kV Glacios transmission electron microscope. Cryo-EM data were collected in two separate sessions on a Titan Krios G2 300 kV transmission electron microscope (Thermo Fisher Scientific) with a post-GIF K3 summit direct electron detector (Gatan) using SerialEM⁶⁰. The target defocus was set to -1.0 to -2.0 µm. Five exposures per 2 µm hole were recorded as movies with 40 frames in super-resolution mode at a physical pixel size of 0.832 Å for a total of about 1.4 s with a dose rate of 34.7–36.1 e⁻·Å⁻² s⁻¹, yielding a total electron dose of 50–51 e⁻·Å⁻².

Cryo-EM data processing and model building of loaded MCM single and double hexamers. All processing steps were performed using CryoSPARC v4^{63,68}. Raw movies were pre-processed using CryoSPARC Live, which included motion correction, Fourier cropping to 0.5, and estimation of contrast transfer function (CTF) parameters. Particles were picked in CryoSPARC v4 using the blob pick tuner function, extracted with a box size of 600 × 600 pixels, and Fourier-cropped to a box size of 300 × 300 pixels, resulting in a pixel size of 1.664 Å. Iterative 2D classification in CryoSPARC v4 was used to remove ‘junk’ particles from each of the two datasets. Subsequently, particles from both datasets were combined and subjected to additional rounds of 2D classification, followed by ab initio reconstruction and heterogeneous refinement, which yielded a well-resolved 3D volume for the loaded MCM2-7 double hexamer (MCM-DH). Non-MCM-DH particles were further cleaned by 2D classification, which identified a small subset of particles that corresponded to MCM-DH (about 8 K) that were combined with the other MCM-DH particles during subsequent 3D refinement. Non-MCM-DH particles that resembled single MCM2-7 hexamers were used as input for ab initio reconstruction and heterogeneous refinement, which yielded a 3D volume of a closed-ring, single MCM2-7 hexamer with duplex DNA inside the central MCM pore and corresponded to DNA-loaded MCM2-7 single hexamers (MCM-SH). Following 3D refinement, MCM-DH and MCM-SH particles were re-extracted at the original pixel size (0.832 Å) with a box size of 500 × 500 pixels. Final 3D maps were calculated using non-uniform refinement in CryoSPARC v4. CTF refinement improved the resolution of the MCM-DH cryo-EM reconstruction but not of that of the MCM-SH (and was therefore omitted in this case). Cryo-EM maps were sharpened with DeepEMhancer⁶⁹. Resolution values were calculated using gold-standard Fourier shell correlation (FSC) method in CryoSPARC v4 and using 3DFSC^{70,71}.

For model building, one or both hexamers from PDB 7W1Y²⁶ were docked into the cryo-EM map of the loaded MCM-DH and MCM-SH, respectively, using UCSF Chimera^{65,66}. The model was checked in COOT⁷² against the cryo-EM map density and minor model rebuilding performed to fix register shift, to account for minor conformational changes between the MCM-SH and MCM-DH structures, and to update the nucleotide status of the ATPase sites of MCM2-7. The models were real-space refined in PHENIX^{73,74} and validated with MolProbity⁷⁵ (Extended Data Table 1).

Structure determination of purified HsMCM2-7 (pre-loading state)

Cryo-EM sample preparation and data collection. HsMCM2-7 and truncated HsCDT1 were mixed at 1.8 µM and 3.6 µM, respectively, in 25 mM HEPES-KOH (pH 7.5), 300 mM potassium acetate, 10 mM magnesium acetate, 10% glycerol, 1 mM ATP, and 1 mM DTT. After a 10-minute incubation on ice, the sample was crosslinked for 10 min by adding an equal volume (125 µl) of crosslinking buffer (25 mM HEPES-KOH (pH 7.5), 300 mM potassium acetate, 10 mM magnesium acetate, 10% glycerol, 1 mM DTT, and 0.05% glutaraldehyde). Crosslinking was stopped by the addition of 25 µl quenching solution (900 mM Tris-HCl (pH 7.5), 90 mM lysine, 90 mM aspartate). The crosslinked complex was purified by gel filtration chromatography on a Superose 6 Increase 10/300 GL column (Cytiva) equilibrated in 25 mM HEPES-KOH (pH 7.5), 300 mM potassium acetate, 10 mM magnesium acetate, 0.2 mM ATP, and 1 mM DTT. Peak fractions were concentrated to about 0.32 mg ml⁻¹ and 3.5 µl of concentrated sample immediately applied to a Quantifoil R2/1 300 copper mesh grid (Quantifoil Micro Tools GmbH), which had been glow-discharged in a GloQube Plus Glow Discharge System (Quorum Technologies) for 45 s at 25 mA and coated with graphene oxide (Sigma Aldrich) as described in ref. 67. The sample was incubated on the grid for 10 s, blotted for 3 s, and vitrified in liquid ethane using a Vitrobot Mark IV (Thermo Fischer Scientific).

Cryo-EM grids were pre-screened in a 200 kV Glacios transmission electron microscope and then transferred to a 300 kV Titan Krios G2 (Thermo Fischer Scientific) equipped with a post-GIF K3 direct detector (Gatan) for data collection. Forty-frame movies (5 movies per hole) were recorded automatically using SerialEM⁶⁰ in super-resolution mode at a nominal magnification of 105,000x and a physical pixel size of 0.832 Å, targeting a defocus range of 1–2 µm and a total electron dose of 51 electrons per Å².

Cryo-EM data processing and model building. Super-resolution cryo-EM movies were pre-processed in RELION 4.0, which included motion correction with RELION’s implementation of MotionCor2 and 2-fold binning, as well as estimation of CTF parameters with CTFFIND-4.1 (refs. 62,76,77). Particles were picked using RELION’s Laplacian-of-Gaussian filter autopicking implementation, extracted with a box size of 600 × 600 pixels, and downsampled by a factor of 2. Particles were then imported into CryoSPARC v4, which was used for all subsequent processing steps⁶³. Particles were first subjected to iterative 2D classification to identify 330,708 good-quality particles that were used for ab initio reconstruction and 3D refinement to obtain an initial map at 3.88 Å resolution. To resolve heterogeneity, the particles were further subjected to 3D classification into 8 classes. Particles from the three best 3D classes were kept and combined for another round of 3D classification. One of the two classes displayed good density on both MCM2-7 hexamers, and its particles were re-extracted at the original pixel size prior to non-uniform refinement to yield a final map of the open MCM2-7 dimer that was post-processed with DeepEMhancer⁶⁹. To improve the local resolution and map quality of a single MCM2-7 hexamer region, we used C2 symmetry expansion and used this new particle stack for local refinement with a soft-edged mask encompassing one of the MCM2-7 hexamers in the dimer. The resultant 3D volume was post-processed with DeepEMhancer⁶⁹ and used for model building.

For model building, the N- and C-terminal domains of each MCM2-7 subunit from PDB 7W1Y²⁶ were rigid-body docked into the cryo-EM map using UCSF Chimera^{65,66}, manually rebuilt in COOT⁷², and real-space refined in PHENIX^{73,74}. To resolve the dimerization interface in the open MCM2-7 dimer, the refined model of the single, open MCM2-7 hexamer was docked into the cryo-EM map of the open MCM2-7 dimer and re-refined in PHENIX^{73,74}. Both refined models were validated using MolProbity⁷⁵ (Extended Data Table 1).

To ensure MCM2–7 dimerization was not caused by crosslinking, we also collected a cryo-EM dataset of uncrosslinked MCM2–7 in the absence of CDT1 and nucleotide. Cryo-EM grids were prepared by applying 3.5 µl of recombinant *HsMCM2–7* at 1.5 µM concentration onto a glow-discharged (25 s at 25 mA in a GloQube Plus glow discharger) 300-mesh R1.2/1.3 UltraAuFoil grid (Quantifoil Micro Tools) in 25 mM HEPES-KOH (pH 7.5), 300 mM potassium acetate, 1% glycerol, and 1 mM DTT. Excess sample was removed by blotting for 4 s and vitrified as described for the crosslinked sample. Cryo-EM data were collected as done for crosslinked MCM2–7 except that EPU was used for automatic data collection with one exposure per hole and a physical pixel size of 0.825 Å. Data processing was done as described for the crosslinked sample. Two-dimensional classification clearly indicated the presence of open MCM2–7 dimers, although the relative orientations of the two hexamers were more variable and prevented the reconstruction of high-resolution cryo-EM maps.

Structure determination of MCM double hexamers formed by dimerization of independently loaded MCM single hexamers without ORC6

Cryo-EM sample preparation and data collection. MCM double hexamers were formed by dimerization of independently loaded single hexamers in reaction setups as described above. To increase the number of particles sufficient for cryo-EM, protein concentrations for loading MCM single hexamers were increased to 480 nM of ORC1–5 (ORC1(ΔN)) and CDC6, and 120 nM CDT1(ΔN) and MBP–MCM2–7 (MBP–MCM5). Elutions from 20 reactions were combined and concentrated to about 0.14 mg ml⁻¹ for freezing. Three and a half µl sample were incubated on glow-discharged (20 s at 15 mA in a GloQube Plus) Quantifoil R2/1300 copper mesh grid with 2 nm carbon layer (Quantifoil Micro Tools GmbH) for 30 s at 4 °C, blotted for 3 s, and vitrified in liquid ethane using a Vitrobot Mark IV (Thermo Fischer Scientific). Cryo-EM data were collected in a 200 kV Glacios transmission electron microscope (Thermo Fisher Scientific) with K3 summit direct electron detector (Gatan) using SerialEM⁶⁰ and a multi-shot strategy with four exposures per hole. Movies were recorded in super-resolution mode with a total electron dose of about 51 e⁻ Å⁻² across 49 frames (exposure time of 1.57 s), a physical pixel size of 0.868 Å, and a defocus range from -1.0 to -2.0 µm.

Cryo-EM data processing and model building. All processing steps were done in CryoSPARC v4^{63,68}. Raw movies were pre-processed in Cryo-SPARC Live, which included motion correction with Fourier cropping to 0.5 and CTF estimation. Particles were picked using blob picker and extracted with a box size of 300 × 300 pixels after 2× binning, yielding a pixel size of 1.736 Å. Particles were cleaned by iterative 2D classification and used for ab initio reconstruction and heterogeneous refinement. High-quality MCM-DH particles were re-extracted at the original pixel size (0.832 Å) for 3D refinement. The cryo-EM map was sharpened with DeepEMhancer⁶⁹. For model building, the MCM-DH structure obtained from normal loading reactions (PDB 8WOF) was docked into the cryo-EM map, minimally adjusted in COOT⁷², and real-space refined in PHENIX^{73,74} (Extended Data Table 1).

Structure analysis

Structures were visualized and figures rendered using PyMOL (The PyMOL Molecular Graphics System, Schrödinger), UCSF Chimera^{65,66}, and UCSF Chimera X⁷⁸. Structural modelling of interactions between ORC3, ORC6, and MCM were done using AlphaFold Multimer^{79,80} and AlphaFold 3⁸¹.

Statistics and reproducibility

A minimum of three independent replicates with similar results were performed for all MCM2–7 loading assay experiments shown as SDS-PAGE or fluorescent measurements (Figs. 1b,d, 2a,e, 5f and 6b

and Extended Data Figs. 1b–g, 2a,b,f, 3m and 9f,h). Three independent replicates with a minimum of ten micrographs per replicate (minimum of $n = 30$) were used for quantifying MCM2–7 double hexamers by negative-stain EM in loading assay eluates (Figs. 2c,f, 4e, 5h and 6c and Extended Data Figs. 2g and 9j–l). Example micrograph regions or class averages (Figs. 1c, 2b, 4f and 5g,i and Extended Data Figs. 1a,f, 3n and 9g,m,n) were obtained from images across at least three independent experimental replicates. Negative-stain EM imaging of purified *HsMCM2–7* (Extended Data Figs. 9a–c) was done independently twice with similar results across at least three micrographs per repeat. For negative-stain EM analyses and quantification of MCM2–7 loading intermediates (Figs. 3c,d, 4a,b, 5c and 6d and Extended Data Figs. 3b,h), a minimum of two independent repeat experiments were performed, with 100–150 micrographs analysed for each with similar results.

Reporting summary

Further information on research design is available in the Nature Portfolio Reporting Summary linked to this article.

Data availability

The PDB coordinates and cryo-EM maps have been deposited into the Protein Data Bank and Electron Microscopy Data Bank under the following accession numbers: PDB 8WOE and EMD-43707 for the loaded human MCM2–7 single hexamer, PDB 8WOF and EMD-43708 for the loaded human MCM2–7 double hexamer, PDB 8WOG and EMD-43709 for human MCM2–7 dimers, PDB 8WOI and EMD-43710 for the locally refined map containing one copy of the human MCM2–7 hexamer from the dimer, and PDB 9CAQ and EMD-45400 for human MCM2–7 double hexamers formed by dimerization of independently loaded MCM single hexamers without ORC6. The previously published model of human MCM-DH and the human ORC used for initial model building and docking are available in the Protein Data Bank using accession codes 7W1Y and 7JPO, respectively. The coordinates and cryo-EM maps of the *S. cerevisiae* MO can be accessed using accession codes PDB 6RQC and EMD-4980. *S. cerevisiae* coordinates for pre-insertion OCCM and OCCM are at PDB 6WGG and PDB 5V8F. Source data are provided with this paper.

59. Gradia, S. D. et al. MacroBac: new technologies for robust and efficient large-scale production of recombinant multiprotein complexes. *Methods Enzymol.* **592**, 1–26 (2017).
60. Mastronarde, D. N. Automated electron microscope tomography using robust prediction of specimen movements. *J. Struct. Biol.* **152**, 36–51 (2005).
61. Zhang, K. Gctf: real-time CTF determination and correction. *J. Struct. Biol.* **193**, 1–12 (2016).
62. Kimanis, D., Dong, L., Sharov, G., Nakane, T. & Scheres, S. H. W. New tools for automated cryo-EM single-particle analysis in RELION-4.0. *Biochem. J.* **478**, 4169–4185 (2021).
63. Punjani, A., Rubinstein, J. L., Fleet, D. J. & Brubaker, M. A. cryoSPARC: algorithms for rapid unsupervised cryo-EM structure determination. *Nat. Methods* **14**, 290–296 (2017).
64. Jaremko, M. J., On, K. F., Thomas, D. R., Stillman, B. & Joshua-Tor, L. The dynamic nature of the human origin recognition complex revealed through five cryoEM structures. *eLife* **9**, e58622 (2020).
65. Pettersen, E. F. et al. UCSF Chimera—a visualization system for exploratory research and analysis. *J. Comput. Chem.* **25**, 1605–1612 (2004).
66. Goddard, T. D., Huang, C. C. & Ferrin, T. E. Visualizing density maps with UCSF Chimera. *J. Struct. Biol.* **157**, 281–287 (2007).
67. Cheng, K., Wilkinson, M., Chaban, Y. & Wigley, D. B. A conformational switch in response to Chi converts RecBCD from phage destruction to DNA repair. *Nat. Struct. Mol. Biol.* **27**, 71–77 (2020).
68. Punjani, A., Zhang, H. & Fleet, D. J. Non-uniform refinement: adaptive regularization improves single-particle cryo-EM reconstruction. *Nat. Methods* **17**, 1214–1221 (2020).
69. Sanchez-Garcia, R. et al. DeepEMhancer: a deep learning solution for cryo-EM volume post-processing. *Commun. Biol.* **4**, 874 (2021).
70. Scheres, S. H. & Chen, S. Prevention of overfitting in cryo-EM structure determination. *Nat. Methods* **9**, 853–854 (2012).
71. Tan, Y. Z. et al. Addressing preferred specimen orientation in single-particle cryo-EM through tilting. *Nat. Methods* **14**, 793–796 (2017).
72. Emsley, P., Lohkamp, B., Scott, W. G. & Cowtan, K. Features and development of Coot. *Acta Crystallogr. D* **66**, 486–501 (2010).
73. Adams, P. D. et al. PHENIX: a comprehensive Python-based system for macromolecular structure solution. *Acta Crystallogr. D* **66**, 213–221 (2010).
74. Afonine, P. V. et al. Real-space refinement in PHENIX for cryo-EM and crystallography. *Acta Crystallogr. D* **74**, 531–544 (2018).

Article

75. Chen, V. B. et al. MolProbity: all-atom structure validation for macromolecular crystallography. *Acta Crystallogr. D.* **66**, 12–21 (2010).
76. Zivanov, J., Nakane, T. & Scheres, S. H. W. A Bayesian approach to beam-induced motion correction in cryo-EM single-particle analysis. *IUCrJ* **6**, 5–17 (2019).
77. Rohou, A. & Grigorieff, N. CTFFIND4: Fast and accurate defocus estimation from electron micrographs. *J. Struct. Biol.* **192**, 216–221 (2015).
78. Goddard, T. D. et al. UCSF ChimeraX: Meeting modern challenges in visualization and analysis. *Protein Sci.* **27**, 14–25 (2018).
79. Evans, R. et al. Protein complex prediction with AlphaFold-Multimer. Preprint at *bioRxiv* <https://doi.org/10.1101/2021.10.04.463034> (2022).
80. Schmid, E. W. & Walter, J. C. Predictomes: a classifier-curated database of AlphaFold-modeled protein-protein interactions. Preprint at *bioRxiv* <https://doi.org/10.1101/2024.04.09.588596> (2024).
81. Abramson, J. et al. Accurate structure prediction of biomolecular interactions with AlphaFold 3. *Nature* **630**, 493–500 (2024).
82. Kawasaki, Y., Kim, H. D., Kojima, A., Seki, T. & Sugino, A. Reconstitution of *Saccharomyces cerevisiae* prereplicative complex assembly in vitro. *Genes Cells* **11**, 745–756 (2006).
83. Wu, M., Lu, W., Santos, R. E., Frattini, M. G. & Kelly, T. J. Geminin inhibits a late step in the formation of human pre-replicative complexes. *J. Biol. Chem.* **289**, 30810–30821 (2014).

Acknowledgements Cryo-EM data were collected at the Yale Cryo-EM resource and at the Laboratory for BioMolecular Structure (LBMS). The authors thank S. Wu, J. Lin, L. Wang, G. Hu and J. Kaminsky for assistance with microscope operation and data collection; H. Marzano

for help with initial model building of the MCM dimer; and M. Hochstrasser, M. Solomon and members of the Bleichert laboratory for critical reading of the manuscript. This work is supported by the National Institutes of General Medicine (R01-GM141313 to F.B.). O.H. is supported by the NIH predoctoral programme in Biophysics (T32-GM008283) and the National Cancer Institute (1F31-CA278331-01). LBMS is supported by the DOE Office of Biological and Environmental Research (KP1607011). The Yale Cryo-EM Resource is funded in part by NIH grant S10OD023603.

Author contributions F.B. conceptualized and supervised the project. R.Y., O.H., M.W. and F.B. cloned expression constructs and purified recombinant proteins. R.Y. and O.H. prepared samples and collected negative-stain EM and cryo-EM data. R.Y., O.H. and F.B. performed biochemical experiments, processed EM data, built and refined atomic models and wrote the manuscript.

Competing interests The authors declare no competing interests.

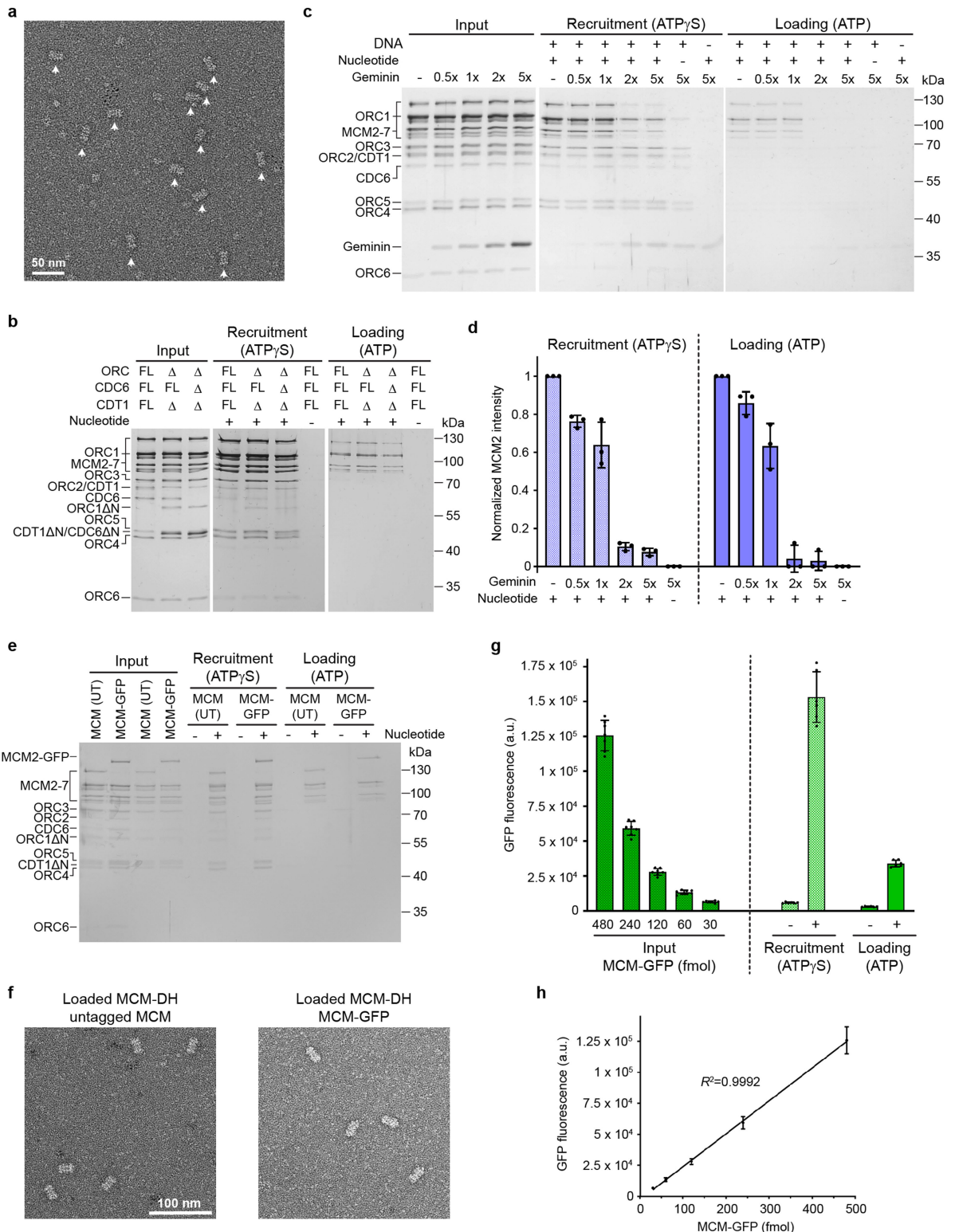
Additional information

Supplementary information The online version contains supplementary material available at <https://doi.org/10.1038/s41586-024-08237-8>.

Correspondence and requests for materials should be addressed to Franziska Bleichert.

Peer review information *Nature* thanks the anonymous reviewer(s) for their contribution to the peer review of this work.

Reprints and permissions information is available at <http://www.nature.com/reprints>.

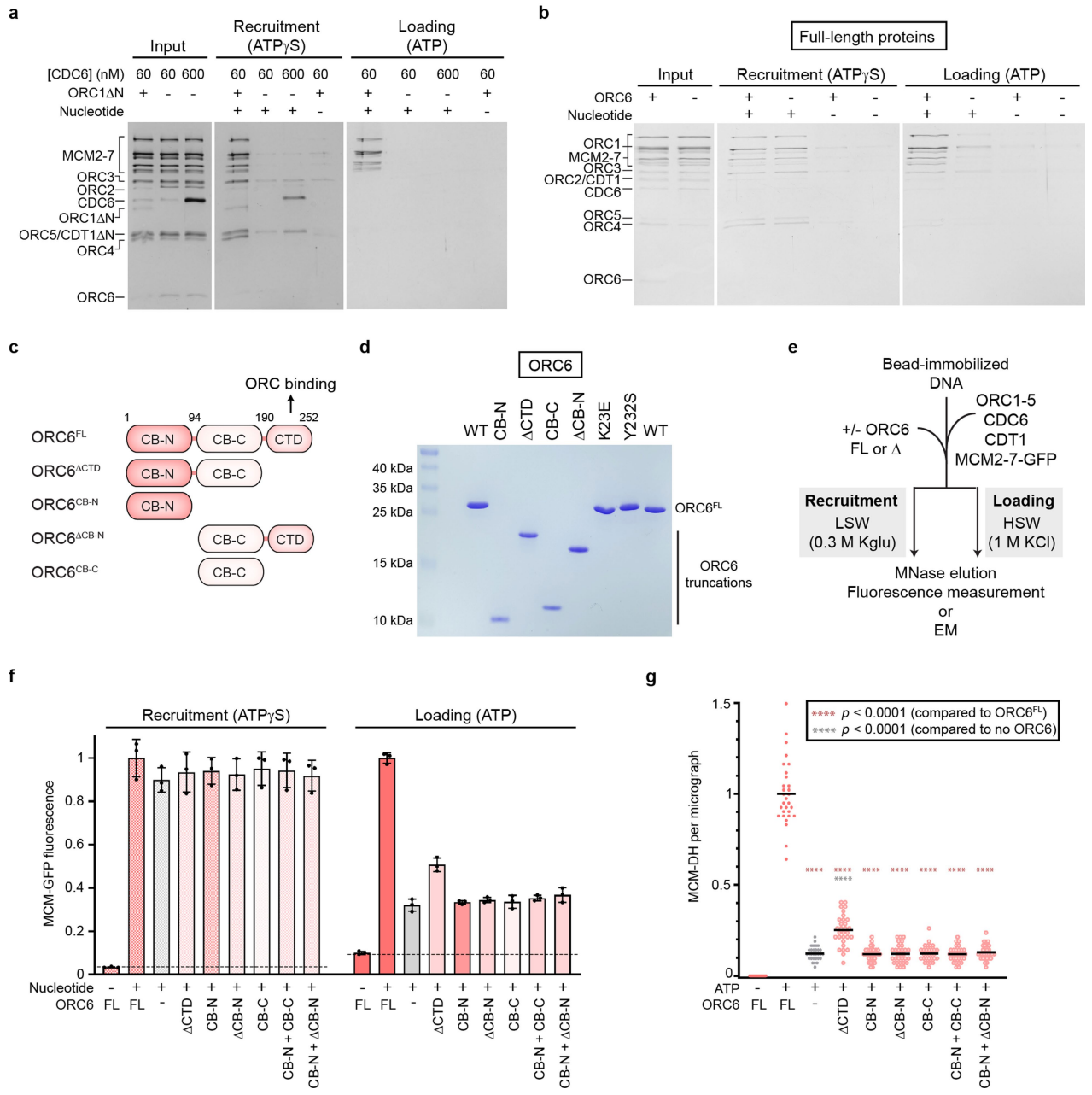


Extended Data Fig. 1 | See next page for caption.

Article

Extended Data Fig. 1 | In vitro reconstitution of human origin licensing and validation of fluorescence-based MCM loading assay. **a)** Electron micrograph of negatively stained particles from high-salt wash eluate of loading reactions with ATP. White arrows mark MCM double hexamers. **b)** N-terminal, intrinsically disordered regions (IDRs) in ORC1, CDC6, and CDT1 are not essential for human MCM loading. Silver-stained SDS-PAGE gels for bead-based MCM recruitment and loading assays are shown. N-terminally truncated ORC1 and CDT1 were used in all subsequent experiments unless noted otherwise. FL, full-length; Δ, truncated. **c** and **d**) Geminin inhibits MCM recruitment and loading in the in vitro reconstituted system. **c)** Silver-stained SDS-PAGE gels of inputs, recruited, and loaded proteins in the absence or presence of increasing concentrations of Geminin (labeled as molar fold excess compared to CDT1). Note that Geminin associates nonspecifically with beads in low-salt conditions.

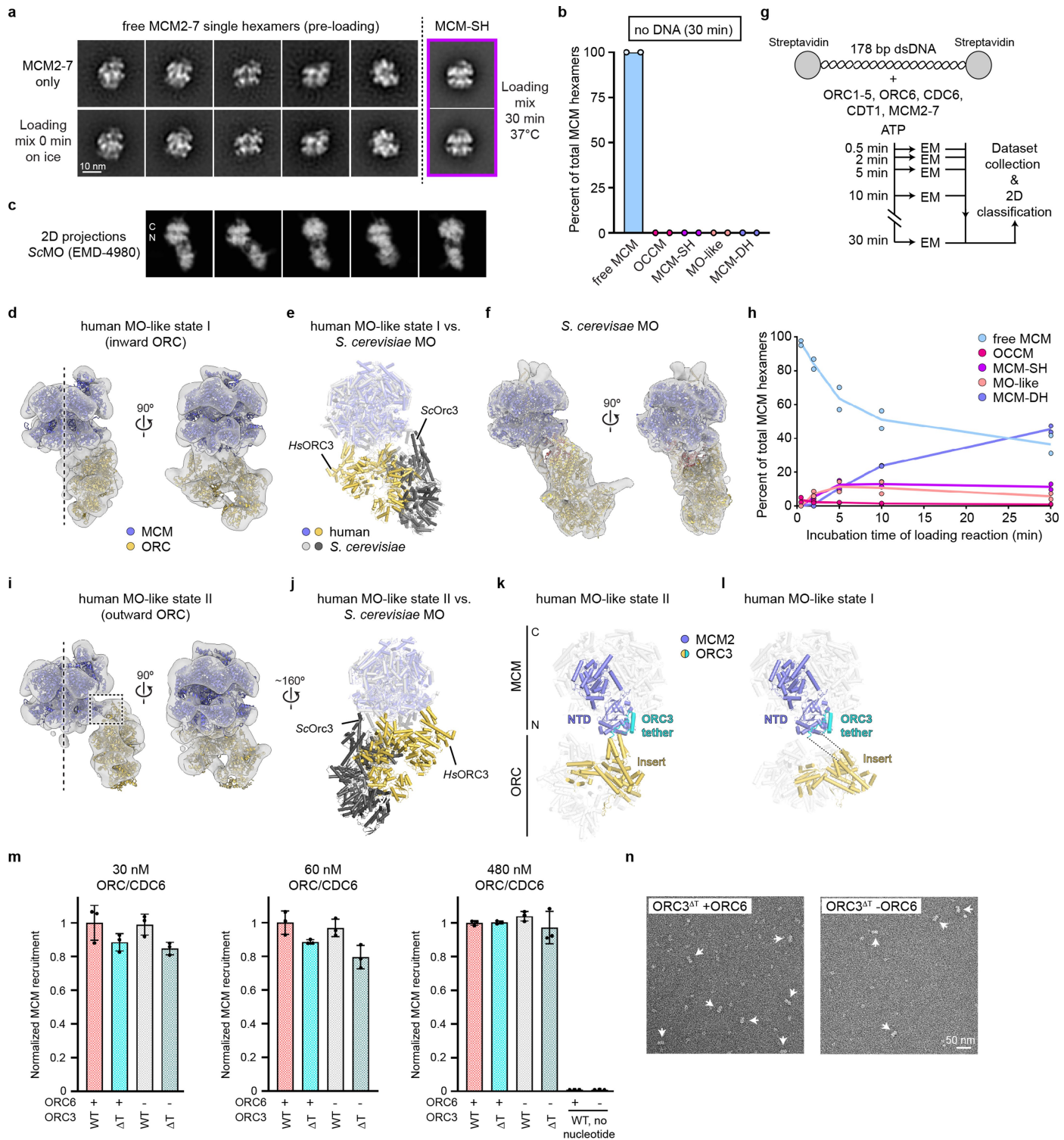
Full-length ORC and CDT1 were used in this experiment. **d)** Quantification of results in **c**. Means and standard deviations of MCM2 band intensities from three independent experiments normalized to the reaction without Geminin on each gel are plotted. **e** to **h**) Validation of fluorescence-based MCM loading assay. **e)** MCM2-7 with GFP fused to the C-terminus of MCM2 supports MCM recruitment and loading to similar levels as untagged (UT) MCM. Silver-stained SDS-PAGE gel is shown. **f)** Loaded MCM-GFP are double hexamers like untagged MCM2-7 as seen in negative-stain EM images of particles eluted from beads. **g)** Raw GFP fluorescence intensities in inputs and elutions from recruitment and loading reactions with MCM-GFP. **h)** The fluorescence intensity signal linearly increases with MCM-GFP concentration. Means and standard deviations from six independent experiments are plotted in **g** and **h**. a.u., arbitrary units. For gel source data, see Supplementary Information.



Extended Data Fig. 2 | Full-length ORC6 facilitates while ORC1 is essential for human MCM loading. **a**) Silver-stained SDS-PAGE gels of inputs and elutions from bead-based recruitment and loading reactions with and without ORC1. **b**) Silver-stained SDS-PAGE gels of elutions from bead-based recruitment and loading reactions with full-length human loading factors with or without ORC6. **c to g**) All ORC6 domains are required *in cis* to enhance human MCM loading. **c**) Domain architecture of human (*Hs*) ORC6. Numbers denote amino acid positions of domain boundaries. Truncated *Hs*ORC6 constructs are schematized below. **d**) SDS-PAGE gel of purified full-length (FL) wild-type (WT), truncated, and mutant ORC6 proteins used in this study. **e**) Experimental setup for assessing the contributions of ORC6 domains to MCM loading. **f**) MCM loading but not recruitment is impaired when ORC6 is absent or truncated. Means and standard deviations of MCM-GFP fluorescence in elutions of bead-based recruitment and loading assays (normalized to the average signal obtained with full-length ORC6) from three independent experiments are plotted. Dashed lines mark background signal in reactions without nucleotide. **g**) Quantification of MCM-DHs observed by EM in elutions of loading reactions (after high-salt wash). The numbers of double hexamers per micrograph were counted manually from three independent experiments, with 10 micrographs recorded for each sample per experimental repeat (total $n = 30$ micrographs per sample), and normalized to the +ORC6-FL sample. Black lines represent means. Statistical significance was determined using two-way ANOVA analysis and the Tukey's multiple comparisons test (***) $P < 0.0001$. Differences in MCM loading efficiencies without ORC6 and with ORC6 truncations between **f** and **g** are likely due to the presence of loaded MCM single hexamers that contribute to the signal measured in the fluorescence-based assay, thus slightly overestimating MCM loading efficiency. For gel source data, see Supplementary Information.

obtained with full-length ORC6) from three independent experiments are plotted. Dashed lines mark background signal in reactions without nucleotide. **g**) Quantification of MCM-DHs observed by EM in elutions of loading reactions (after high-salt wash). The numbers of double hexamers per micrograph were counted manually from three independent experiments, with 10 micrographs recorded for each sample per experimental repeat (total $n = 30$ micrographs per sample), and normalized to the +ORC6-FL sample. Black lines represent means. Statistical significance was determined using two-way ANOVA analysis and the Tukey's multiple comparisons test (***) $P < 0.0001$. Differences in MCM loading efficiencies without ORC6 and with ORC6 truncations between **f** and **g** are likely due to the presence of loaded MCM single hexamers that contribute to the signal measured in the fluorescence-based assay, thus slightly overestimating MCM loading efficiency. For gel source data, see Supplementary Information.

Article

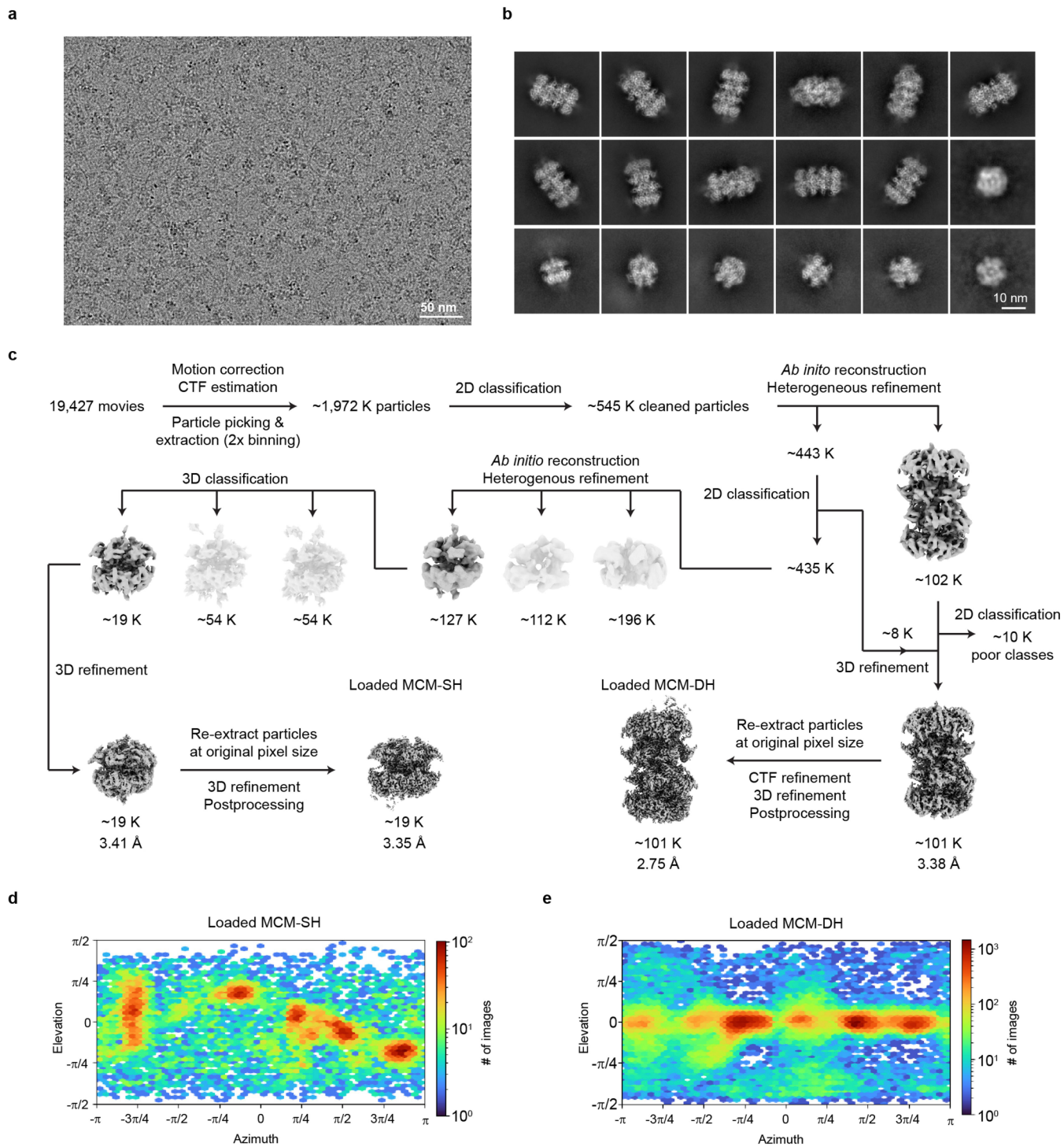


Extended Data Fig. 3 | See next page for caption.

Extended Data Fig. 3 | The human MO-like complex adopts different conformational states that are architecturally distinct from the *S. cerevisiae* (Sc) MO. **a**) Class averages (negative stain) of purified human MCM2-7 or of loading reactions kept on ice. **b**) Quantification of MCM-containing assemblies (by negative-stain EM and 2D classification) in loading reactions without DNA. **c**) Projections of the ScMO cryo-EM map (EMD-4980⁵, low-pass filtered to 20 Å). **d**) Negative-stain EM reconstruction of human MO-like complex state I, with structures of human MCM-SH (this study or PDB 7W1Y²⁶) and human ORC (PDB 7JPO⁶⁴) docked into the EM map. **e**) Superposition of MCMs in ScMO and human MO-like complex state I. The ORC6-binding regions in the ORC3 inserts are marked for reference. **f**) Low-pass filtered (to 15 Å) cryo-EM map of ScMO (EMD-4980 with PDB 6RQC⁵). **g–h**) The MO-like complex peaks early during MCM loading. **g**) Experimental workflow. **h**) Quantification of MCM-containing assemblies. **i**) Negative-stain EM reconstruction of human MO-like complex

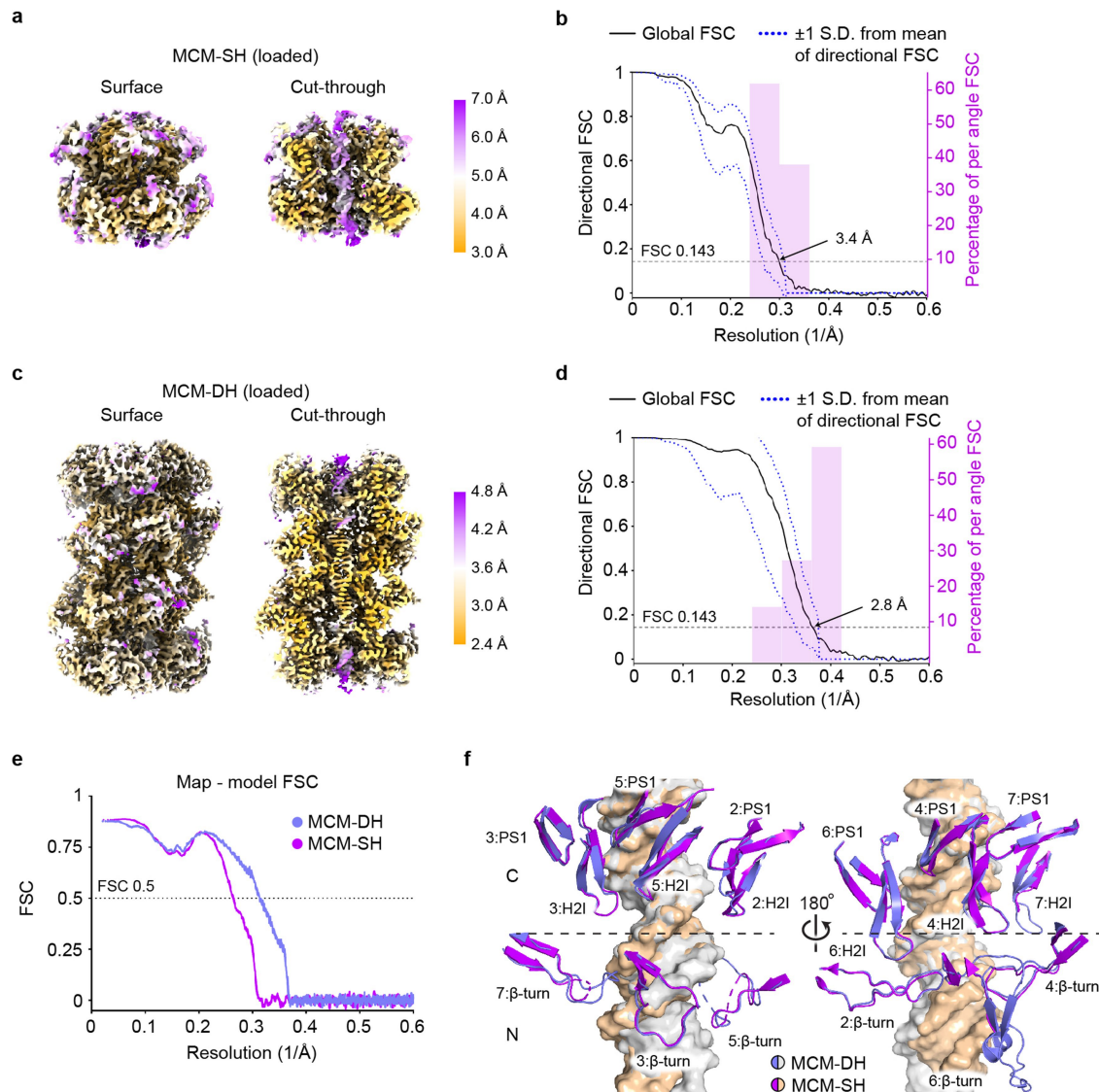
state II with MCM and ORC docked (as in **d**). **j**) Superposition of MCMs in ScMO and human MO-like complex state II. **k–l**) The ORC3 insert is positioned closer to the MCM2-NTD in MO state II (in **k**) than in MO state I (in **l**). Dashed lines in **l** indicate distances between consecutive amino acids if the ORC3 tether were to remain bound to MCM2. This interaction site is delineated by a dashed box in **i**. **m**) Deletion of the ORC3 tether sustains efficient MCM recruitment to DNA. Means and standard deviations of MCM-GFP fluorescence in bead-based recruitment assays from three independent experiments, normalized to the average of ORC3(WT)/+ORC6 reactions at each ORC/CDC6 concentration. **n**) Negative-stain electron micrograph region of MCM-DHs (white arrows) eluted from beads after high-salt wash from loading reactions with ORC3(ΔT). In **b** and **h**, two independent experiments with 100–150 micrographs each were analyzed per condition.

Article



Extended Data Fig. 4 | Cryo-EM data processing and validation of loaded human MCM2-7. **a)** Cryo-EM image and **b)** 2D cryo-class averages from human MCM loading reactions. **c)** Cryo-EM data processing workflow for MCM single

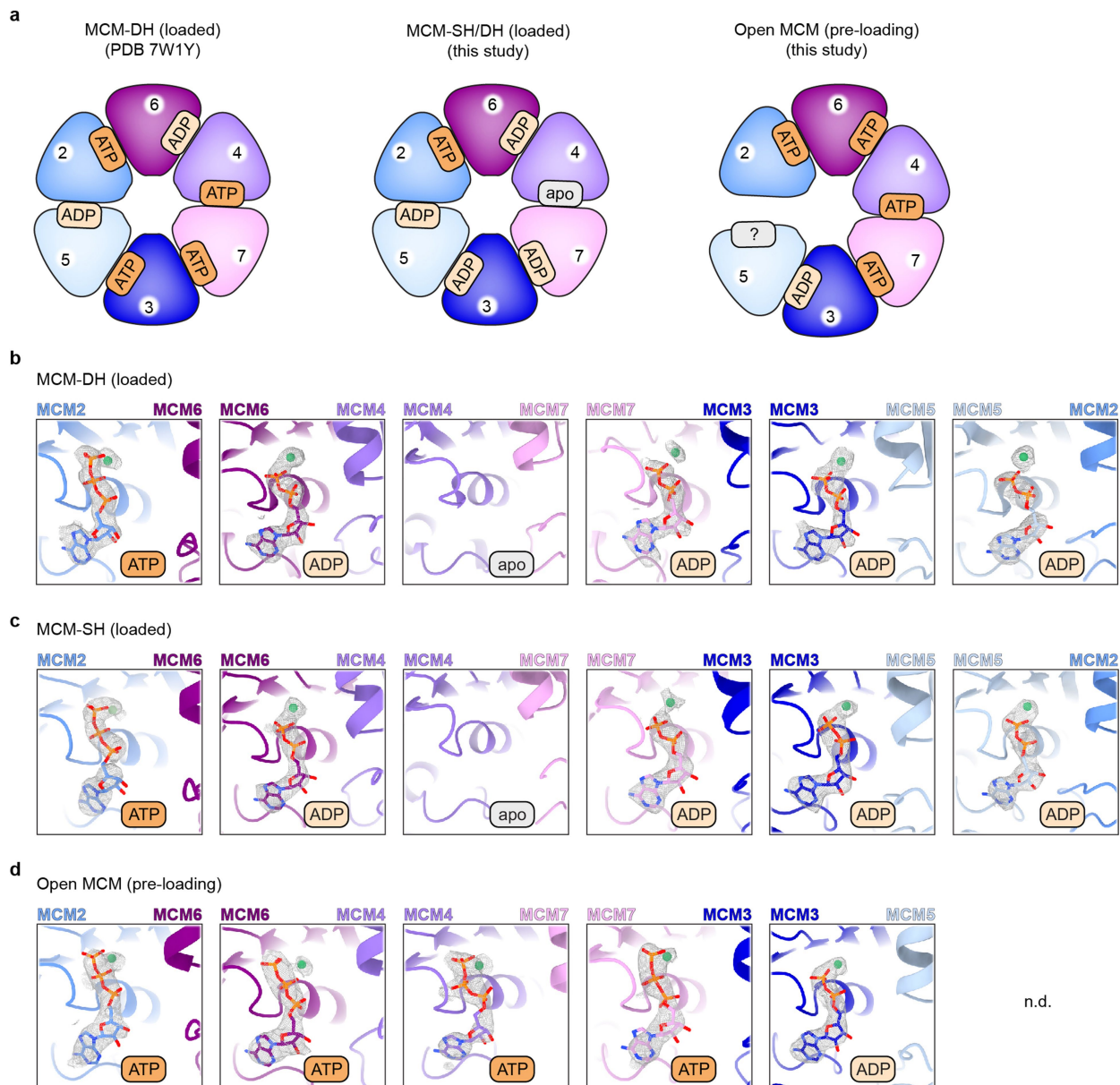
and double hexamer reconstructions. **d** and **e**) Angular distribution plots for reconstructed cryo-EM volumes of loaded MCM single (in **d**) and double (in **e**) hexamers.



Extended Data Fig. 5 | Resolution estimation of loaded human MCM-SH and MCM-DH cryo-EM reconstructions. **a)** Surface and cut-through views of unsharpened cryo-EM map of loaded MCM single hexamer. **b)** 3D Fourier shell correlation (FSC) plot for loaded MCM single hexamer reconstruction. **c)** Surface and cut-through views of unsharpened cryo-EM map of loaded MCM double hexamer. **d)** 3D FSC plot for loaded MCM double hexamer

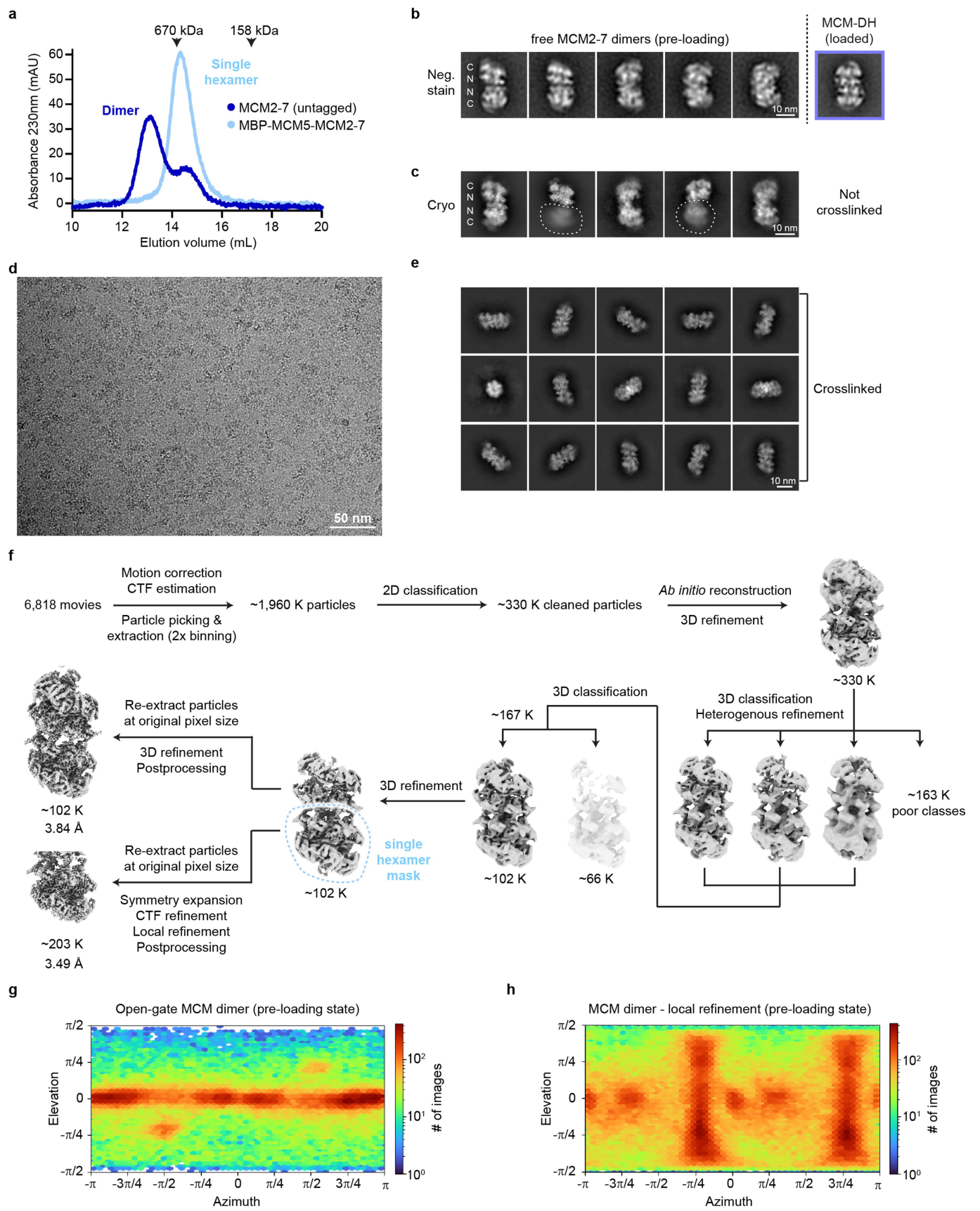
reconstruction. **e)** FSC curves of cryo-EM maps and refined models. **f)** Interior hairpin loop interactions with DNA are similar in MCM-DH and MCM-SH. Helix-2-insert (H2I), pre-sensor 1 β hairpin (PS1), and β -turn loops in each subunit are shown as cartoon and DNA is shown as surface. The β -turn loops in MCM5 of both MCM-DH and MCM-SH, the H2I and β -turn loops in MCM7 of MCM-SH, and the β -turn loop in MCM6 of MCM-SH are partially or mostly disordered.

Article



Extended Data Fig. 6 | Nucleotide-binding states within human MCM2-7 before and after loading onto DNA. a) Comparison of nucleotide occupancies at the AAA+ interfaces in the loaded MCM single and double hexamers and the open-gate MCM2-7 dimer (pre-loading state) observed in this study with those in the previously published human MCM double hexamer structure (PDB 7W1Y²⁶). ATPase sites are viewed from the N-terminal MCM tier. **b to d**) Zoomed views of the ATP binding sites in the loaded MCM double hexamer (in **b**),

the loaded MCM2-7 single hexamer (in **c**), and open-gate MCM2-7 dimer in the pre-loading state (in **d**). ATP and magnesium are shown in stick representation and as spheres, respectively, with corresponding cryo-EM map density as grey mesh. Note that the nucleotide occupancy at the MCM2/5 site in the open-gate MCM2-7 (in **d**) could not be determined (n.d.) due to poor map quality in this region.

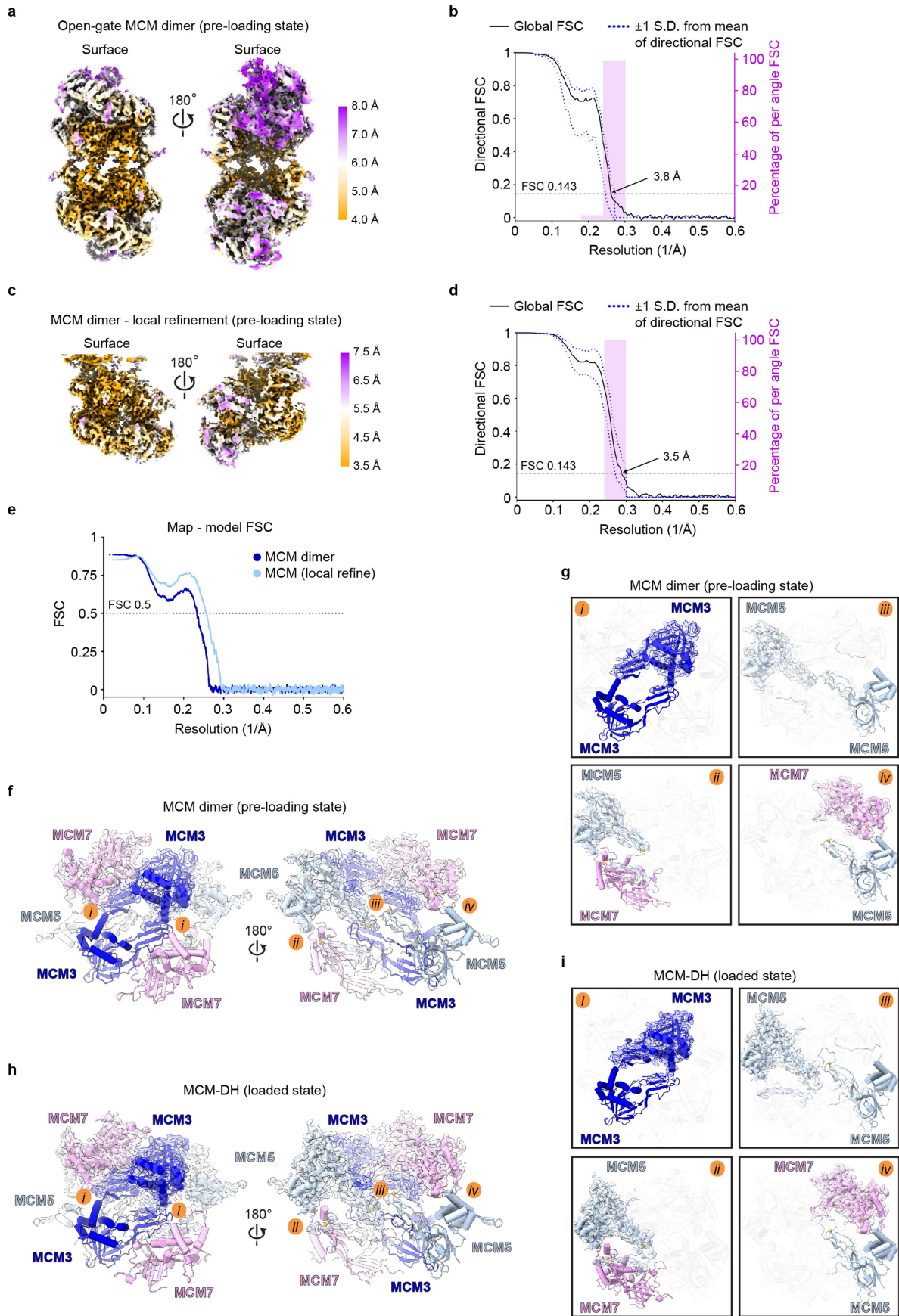


Extended Data Fig. 7 | See next page for caption.

Article

Extended Data Fig. 7 | Open-ring human MCM2-7 hexamers can dimerize without loading onto DNA. **a**) Size exclusion chromatography of purified human MCM2-7 shows predominant dimerization of MCM2-7 hexamers (untagged). Fusing MBP to the N-terminus of MCM5 prevents dimer formation. The elution of molecular weight markers (thyroglobulin – 670 kDa, γ-globulin – 158 kDa) is indicated by arrowheads. **b**) Negative-stain EM 2D class averages of MCM2-7 dimers, which are structurally distinct from loaded MCM double hexamers (class average shown for comparison). **c to h**) Cryo-EM data processing and validation of human MCM2-7 dimers. **c**) Cryo-EM 2D class averages of MCM2-7 dimers without crosslinking. Fuzzy density (outlined by dotted line)

indicates conformational flexibility between both hexamers in the MCM dimer. **d**) Cryo-EM image and **e**) 2D cryo-EM class averages of crosslinked (with glutaraldehyde) MCM dimers. **f**) Cryo-EM data processing workflow for 3D reconstruction. **g** and **h**) Angular distribution plots for the MCM2-7 dimer (in **g**, C1 refined) and the locally refined, symmetry expanded MCM2-7 hexamer (in **h**). We note that although MCM2-7 was mixed with CDT1 prior to cryo-EM sample preparation, no density is observed for this licensing factor, consistent with prior findings that the human proteins, unlike the *S. cerevisiae* counterparts^{8,82}, do not stably co-associate into an MCM2-7•Cdt1 heptamer⁸³.

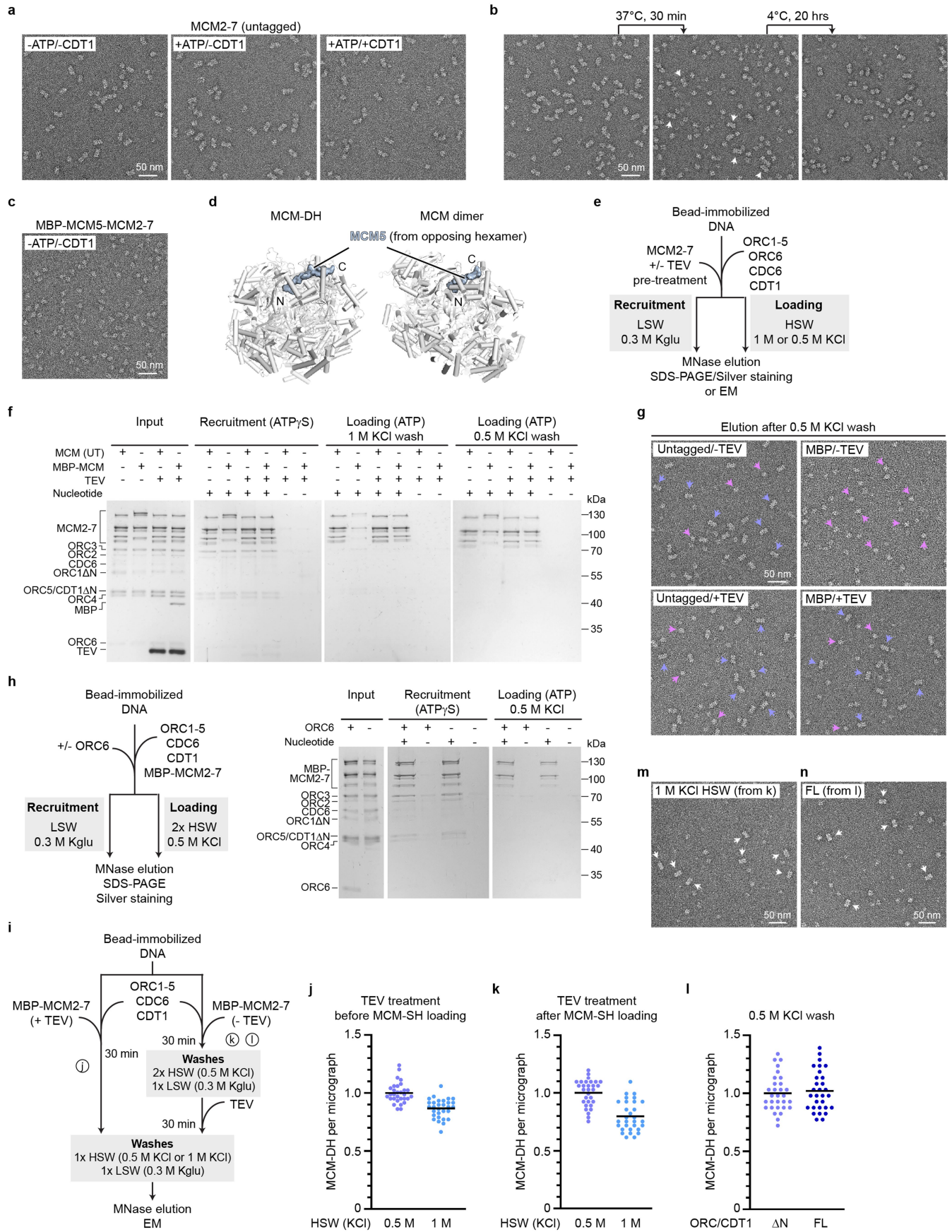


Extended Data Fig. 8 | See next page for caption.

Article

Extended Data Fig. 8 | Resolution estimation of MCM2-7 cryo-EM reconstructions in the pre-loading state and structural comparison with the loaded MCM double hexamer. **a**) Surface view of sharpened cryo-EM map of the full MCM dimer. **b**) 3D FSC plot for cryo-EM reconstruction of the full MCM dimer. **c**) Surface view of sharpened cryo-EM map of locally refined MCM hexamer in the MCM dimer. **d**) 3D FSC plot for cryo-EM reconstruction of locally refined MCM dimer map. **e**) FSC curves comparing cryo-EM maps and refined models. **f to i**) The MCM dimer is stabilized by similar interactions

between MCM3, MCM5, and MCM7 as in the loaded MCM double hexamer. **f and g**) MCM5/3/7 dimerization interface in the open-gate MCM dimer. A structure overview is shown in **f** and zoomed views of the contact sites between subunits in the two hexamers (*i-iv*) in **g**. **h and i**) MCM5/3/7 dimerization interface in the loaded MCM double hexamer. A structure overview is shown in **h** and zoomed views of the contact sites between subunits in the two hexamers (*i-iv*) in **i**. MCM subunits are shown as cartoon, with transparent cryo-EM map density overlaid in one of the hexamers.

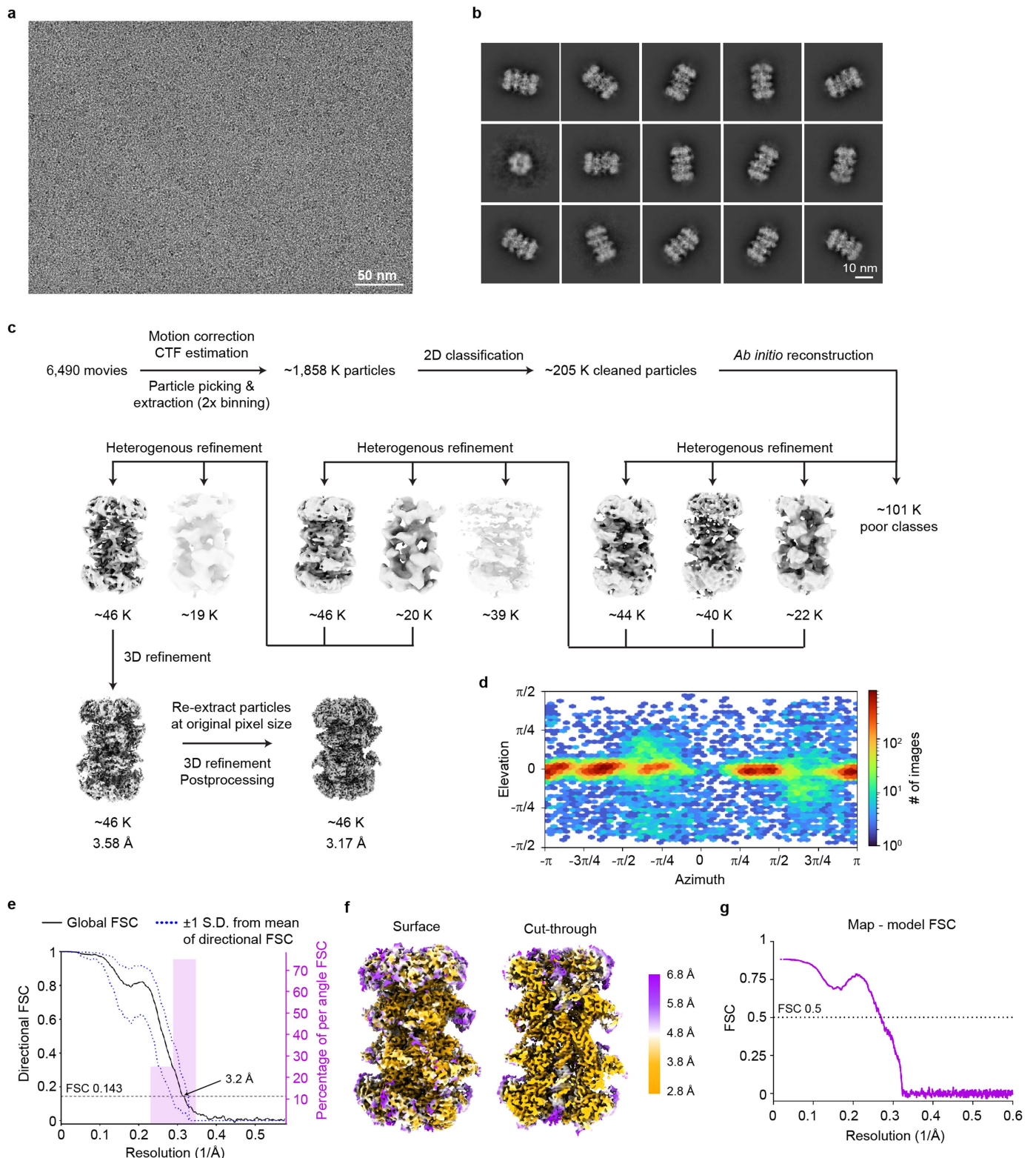


Extended Data Fig. 9 | See next page for caption.

Article

Extended Data Fig. 9 | Human MCM2-7 can dimerize on DNA in the absence of other loading factors. **a)** MCM2-7 dimers with and without nucleotide or CDT1. Incubations were done on ice. **b)** MCM2-7 dimers and monomers are in a temperature-regulated equilibrium, with a subset of MCM2-7 remaining in the dimeric form (arrowheads) at 37 °C. **c)** MCM2-7 with an MBP-TEV tag at the N-terminus of MCM5 is monomeric (on ice). Subregions of negative-stain electron micrographs are shown in **a–c**. **d)** The MCM5 N-terminus of one hexamer is buried in the adjacent hexamer in both the MCM dimer and loaded MCM-DH. **e–h)** MBP-MCM5 supports loading of MCM-SHs but not MCM-DH formation. **e)** Experimental workflow. **f)** Silver-stained SDS-PAGE gels of inputs and elutions from recruitment and loading reactions with untagged (UT) or MBP-MCM5 MCM2-7 assemblies, either with or without pre-incubation of MCM2-7 with TEV. **g)** Subregions of negative-stain electron micrographs of elutions from reactions in **f**. MCM-SH and MCM-DH are marked by magenta

and blue arrowheads. **h)** ORC6 is not required for MCM-SH loading. Left: Experimental setup. Right: Silver-stained SDS-PAGE gels of reactions with MBP-MCM2-7 without or with ORC6. **i)** Workflow for experiments in **j–l**. **j)** Quantification of MCM-DH particles eluted after 0.5 M or 1 M KCl washes. MBP-MCM was pre-treated with TEV before the loading reaction. **k)** Quantification of MCM-DH particles eluted after 0.5 M or 1 M KCl washes. MCM-SH were first loaded and dimerization initiated by TEV cleavage after removal of ORC, CDC6, CDT1, and free MCM. **l)** Quantification of MCM-DH particles formed by dimerization of independently loaded MCM-SH, loaded either with full-length (FL) or truncated (Δ) ORC and CDT1. $n = 10$ electron micrographs for each of three independent experiments in **j–l** (total $n = 30$). Black lines represent means in **j–l**. **m–n)** Subregion of electron micrographs from **k** and **l** showing MCM-DHs (white arrows). For gel source data, see Supplementary Information.



Extended Data Fig. 10 | Cryo-EM data processing and validation of human MCM2-7 formed by dimerization of independently loaded MCM single hexamers in the absence of other loading factors. **a)** Representative cryo-EM image. **b)** 2D cryo-class averages of MCM-DH. **c)** Workflow of cryo-EM data processing. **d)** Angular distribution plot for reconstructed cryo-EM volume.

e) 3D FSC plot for MCM-DH reconstruction. **f)** Surface and cut-through views of unsharpened cryo-EM map of MCM-DH formed by dimerization of independently loaded MCM-SHs. **g)** FSC curve comparing cryo-EM map and refined MCM-DH model.

Article

Extended Data Table 1 | Cryo-EM data collection, refinement and validation statistics

	MCM-DH (EMDB-43708) (PDB 8W0F)	MCM-SH (EMDB-43707) (PDB 8W0E)	MCM dimer (EMDB-43709) (PDB 8W0G)	Open-gate MCM (locally refined) (EMDB-43710) (PDB 8W0I)	MCM-DH (dimerization of independently loaded MCM-SH) (EMDB-45400) (PDB 9CAQ)
Data collection and processing					
Magnification	x105,000	x105,000	x105,000	x105,000	x45,000
Voltage (kV)	300	300	300	300	200
Electron exposure (e-/Å ²)	50.96/49.86	50.96/49.86	50.96	50.96	51.54
Defocus range (μm)	-1.0 to -2.0	-1.0 to -2.0	-1.0 to -2.0	-1.0 to -2.0	-1.0 to -2.0
Pixel size (Å)	0.832	0.832	0.832	0.832	0.868
Symmetry imposed	C1	C1	C1	C1 (C2 symmetry expanded)	C1
Initial particle images (no.)	1,972,086	1,972,086	1,960,293	1,960,293	1,857,849
Final particle images (no.)	100,748	18,534	101,722	203,444	46,418
Map resolution (Å)	2.75	3.35	3.84	3.49	3.17
FSC threshold	0.143	0.143	0.143	0.143	0.143
Refinement					
Initial model used (PDB code)	7W1Y	7W1Y	7W1Y	7W1Y	8W0F
Model resolution (Å)	3.2	3.8	4.4	3.9	3.7
FSC threshold	0.5	0.5	0.5	0.5	0.5
Map sharpening <i>B</i> factor (Å ²)	N/A	N/A	N/A	N/A	N/A
Model composition					
Non-hydrogen atoms	63,321	30,082	56,920	28,381	60,375
Protein residues	7,721	3,647	7,134	3,557	7,368
DNA residues	94	50	0	0	88
Ligands (ATP, ADP, Mg, Zn)	2, 8, 10, 10	1, 4, 5, 5	8, 2, 10, 10	4, 1, 5, 5	2, 8, 9, 10
<i>B</i> factors (Å ²)					
Protein	102.19	121.36	292.93	173.08	105.68
DNA	73.80	96.83			85.52
Ligand	92.22	104.53	248.74	157.70	104.68
R.m.s. deviations					
Bond lengths (Å)	0.003	0.002	0.003	0.003	0.007
Bond angles (°)	0.532	0.535	0.611	0.491	0.917
Validation					
MolProbity score	1.72	1.73	1.65	1.53	1.84
Clashscore	6.31	6.90	5.53	4.48	6.65
Poor rotamers (%)	1.08	0.63	0.51	0.03	0.45
Ramachandran plot					
Favored (%)	95.02	94.98	94.96	95.63	92.40
Allowed (%)	4.98	5.02	5.04	4.37	7.60
Disallowed (%)	0.00	0.00	0.00	0.00	0.00

Reporting Summary

Nature Portfolio wishes to improve the reproducibility of the work that we publish. This form provides structure for consistency and transparency in reporting. For further information on Nature Portfolio policies, see our [Editorial Policies](#) and the [Editorial Policy Checklist](#).

Statistics

For all statistical analyses, confirm that the following items are present in the figure legend, table legend, main text, or Methods section.

n/a Confirmed

- The exact sample size (n) for each experimental group/condition, given as a discrete number and unit of measurement
- A statement on whether measurements were taken from distinct samples or whether the same sample was measured repeatedly
- The statistical test(s) used AND whether they are one- or two-sided
Only common tests should be described solely by name; describe more complex techniques in the Methods section.
- A description of all covariates tested
- A description of any assumptions or corrections, such as tests of normality and adjustment for multiple comparisons
- A full description of the statistical parameters including central tendency (e.g. means) or other basic estimates (e.g. regression coefficient) AND variation (e.g. standard deviation) or associated estimates of uncertainty (e.g. confidence intervals)
- For null hypothesis testing, the test statistic (e.g. F , t , r) with confidence intervals, effect sizes, degrees of freedom and P value noted
Give P values as exact values whenever suitable.
- For Bayesian analysis, information on the choice of priors and Markov chain Monte Carlo settings
- For hierarchical and complex designs, identification of the appropriate level for tests and full reporting of outcomes
- Estimates of effect sizes (e.g. Cohen's d , Pearson's r), indicating how they were calculated

Our web collection on [statistics for biologists](#) contains articles on many of the points above.

Software and code

Policy information about [availability of computer code](#)

Data collection EPU 2, SerialEM 4.1

Data analysis MotionCor2 1.6.4, GCTF 1.06, GAUTOMATIC 0.56, RELION 4.0.1, PHENIX 1.21-5207, COOT 0.9.8.1, PyMOL 2.4.0 and 2.6.0, UCSF Chimera 1.16, UCSF ChimeraX 1.5 and 1.6.1, CryoSPARC v4.2.1, Graphad Prism 10, AlphaFold 2/3, ImageJ 1.53t, MolProbity (as implemented in PHENIX 1.21-5207), DeepEMhancer v20220530

For manuscripts utilizing custom algorithms or software that are central to the research but not yet described in published literature, software must be made available to editors and reviewers. We strongly encourage code deposition in a community repository (e.g. GitHub). See the Nature Portfolio [guidelines for submitting code & software](#) for further information.

Data

Policy information about [availability of data](#)

All manuscripts must include a [data availability statement](#). This statement should provide the following information, where applicable:

- Accession codes, unique identifiers, or web links for publicly available datasets
- A description of any restrictions on data availability
- For clinical datasets or third party data, please ensure that the statement adheres to our [policy](#)

The PDB coordinates and cryo-EM maps have been deposited into the Protein Data Bank and Electron Microscopy Data Bank under the following accession numbers: PDB 8W0E and EMD-43707 for the loaded HsMCM2-7 single hexamer, PDB 8W0F and EMD-43708 for the loaded HsMCM2-7 double hexamer, PDB 8W0G

and EMD-43709 for HsMCM2-7 dimers, PDB 8W0I and EMD-43710 for the locally refined map of the HsMCM2-7 hexamer from the dimer, and PDB 9CAQ and EMD-45400 for HsMCM2-7 double hexamers formed by dimerization of independently loaded MCM single hexamers without ORC6.

The previously published model of human MCM-DH and human ORC used for initial model building and docking are available in the Protein Data Bank using accession codes 7W1Y and 7JPO, respectively. The coordinates and cryo-EM maps of the *S. cerevisiae* MO can be accessed using accession code PDB 6RQC and EMD-4980. *S. cerevisiae* coordinates for pre-insertion OCCM and OCCM are PDB 6WGG and PDB 5V8F.

Research involving human participants, their data, or biological material

Policy information about studies with [human participants or human data](#). See also policy information about [sex, gender \(identity/presentation\), and sexual orientation](#) and [race, ethnicity and racism](#).

Reporting on sex and gender

N/A

Reporting on race, ethnicity, or other socially relevant groupings

N/A

Population characteristics

N/A

Recruitment

N/A

Ethics oversight

N/A

Note that full information on the approval of the study protocol must also be provided in the manuscript.

Field-specific reporting

Please select the one below that is the best fit for your research. If you are not sure, read the appropriate sections before making your selection.

Life sciences

Behavioural & social sciences

Ecological, evolutionary & environmental sciences

For a reference copy of the document with all sections, see nature.com/documents/nr-reporting-summary-flat.pdf

Life sciences study design

All studies must disclose on these points even when the disclosure is negative.

Sample size

Sample sizes of cryo-EM datasets are described in Extended Data Table 1 and in Extended Data Figures 4, 7, and 10. The sample sizes were determined based on availability of microscope time and the desired final resolution of cryo-EM maps. For negative-stain EM datasets of MCM loading intermediates, typically ~150 micrographs were collected because this yielded a sufficient number of particles for reliable 2D classification into various classes representing different loading intermediates. For quantification of MCM-DH in bead-based loading assays, a minimum of 30 negative-stain EM micrographs were recorded in total, a sample size adequate based on the distribution of the data to see clearly visible effects. Biochemical experiments were repeated at least three times, which was sufficient to observe effects based on the distribution of the data. No statistical methods were used to predetermine sample size.

Data exclusions

Electron micrographs or movies with high drift, ice contamination, suboptimal ice thickness, or poor staining (for negative-stain EM) were excluded due to their negative impact on the quality of 2D classes and 3D reconstructions. Damaged particles identified during 2D or 3D classification were excluded from further processing. This exclusion procedure is a standard practice during single-particle EM data processing.

Replication

All biochemical experiments were successfully performed at least three times independently with similar results. Negative-stain EM data quantification of intermediate states was done at least twice from independent experiments with consistent results. The number of replication are included in the figure legends. All experiments were reproduced successfully.

Randomization

Cryo-EM particles were randomly split into separate datasets for resolution estimation using the gold-standard Fourier Shell Correlation (FSC). Additional randomization of data is not relevant to this study as assays were not conducted on groups with variable individuals.

Blinding

Blinding is not feasible nor relevant for protein structure determination and the biochemical assays in this study because these results are not subjective.

Reporting for specific materials, systems and methods

We require information from authors about some types of materials, experimental systems and methods used in many studies. Here, indicate whether each material, system or method listed is relevant to your study. If you are not sure if a list item applies to your research, read the appropriate section before selecting a response.

Materials & experimental systems

n/a	Involved in the study
<input checked="" type="checkbox"/>	Antibodies
<input type="checkbox"/>	Eukaryotic cell lines
<input checked="" type="checkbox"/>	Palaeontology and archaeology
<input checked="" type="checkbox"/>	Animals and other organisms
<input checked="" type="checkbox"/>	Clinical data
<input checked="" type="checkbox"/>	Dual use research of concern
<input checked="" type="checkbox"/>	Plants

Methods

n/a	Involved in the study
<input checked="" type="checkbox"/>	ChIP-seq
<input checked="" type="checkbox"/>	Flow cytometry
<input checked="" type="checkbox"/>	MRI-based neuroimaging

Eukaryotic cell linesPolicy information about [cell lines and Sex and Gender in Research](#)

Cell line source(s)

High Five cells (BTI-TN-5B1-4) and SF9 cells (*Spodoptera frugiperda*) from Thermo Fischer Scientific

Authentication

None of the cell lines were authenticated.

Mycoplasma contamination

Mycoplasma contamination was not checked for cell lines.

Commonly misidentified lines
(See [ICLAC](#) register)

None of the cell lines used in the study are listed in the commonly misidentified cell lines.

Plants

Seed stocks

Report on the source of all seed stocks or other plant material used. If applicable, state the seed stock centre and catalogue number. If plant specimens were collected from the field, describe the collection location, date and sampling procedures.

Novel plant genotypes

Describe the methods by which all novel plant genotypes were produced. This includes those generated by transgenic approaches, gene editing, chemical/radiation-based mutagenesis and hybridization. For transgenic lines, describe the transformation method, the number of independent lines analyzed and the generation upon which experiments were performed. For gene-edited lines, describe the editor used, the endogenous sequence targeted for editing, the targeting guide RNA sequence (if applicable) and how the editor was applied.

Authentication

Describe any authentication procedures for each seed stock used or novel genotype generated. Describe any experiments used to assess the effect of a mutation and, where applicable, how potential secondary effects (e.g. second site T-DNA insertions, mosaicism, off-target gene editing) were examined.